

Review

# Exploitation of the Maximum Entropy Principle in the Study of Thermal Conductivity of Silicon, Germanium and Graphene

Giovanni Mascali 

Department of Mathematics and Computer Science, Università degli Studi della Calabria and INFN-Gruppo c. Cosenza, 87036 Cosenza, Italy; g.mascali@unical.it; Tel.: +39-0984-496418

**Abstract:** In this paper, we review the application of a recent formula for the lattice thermal conductivity to silicon and germanium, which are two of the most commonly used materials in electronic devices, and to graphene, one the most promising new materials. The formula, which is based on a hierarchy of macroscopic models that generalize the Cattaneo equation, is capable of reproducing the results achieved by means of the well-known Callaway formula. In semiconductors, energy transport is largely due to acoustic phonons, therefore one can choose suitable moments of their occupation numbers as variables of the models. Equations determining the time evolution of these state variables are derived from the Boltzmann–Peierls transport equation by integration, while the maximum entropy principle (MEP) is used to obtain closure relations for the extra variables. All relevant phonon scattering mechanisms are taken into account. We present numerical results regarding the steady-state and dynamical thermal conductivities of silicon, germanium, and graphene, showing their main characteristics and how these are affected by the various scatterings. The results are in good qualitative and quantitative agreement with those in the literature, confirming that MEP is a valid method for developing macroscopic models of charge and energy transport in semiconductor materials.

**Keywords:** thermal conductivity; moments method; maximum entropy principle; silicon; germanium; graphene



**Citation:** Mascali, G. Exploitation of the Maximum Entropy Principle in the Study of Thermal Conductivity of Silicon, Germanium and Graphene. *Energies* **2022**, *15*, 4718. <https://doi.org/10.3390/en15134718>

Academic Editor: Bertrand Lenoir

Received: 30 May 2022

Accepted: 24 June 2022

Published: 27 June 2022

**Publisher's Note:** MDPI stays neutral with regard to jurisdictional claims in published maps and institutional affiliations.



**Copyright:** © 2022 by the author. Licensee MDPI, Basel, Switzerland. This article is an open access article distributed under the terms and conditions of the Creative Commons Attribution (CC BY) license (<https://creativecommons.org/licenses/by/4.0/>).

## 1. Introduction

In the last decades, scientific interest in and research on the thermal conductivity  $\kappa$  of semiconductor materials have significantly increased [1–9]. Indeed, from a theoretical point of view, since the ability of a material to conduct heat heavily depends on its atomic structure, understanding it is important to gain insight into many other properties of the material. While, from a practical perspective, two contradictory demands have emerged.

On one side, the ongoing miniaturization of electronic components has made heat removal from chips an issue of crucial importance [10–12]. To achieve this aim, it is important to adjust device parameters and geometry in such a way as to make thermal conductivity large enough along appropriate directions. On the other side, a lower thermal conductivity is required to improve the efficiency of solid state energy conversion devices [9,13]. Conversion efficiency can be measured in terms of the dimensionless figure of merit  $ZT = T\sigma S^2/\kappa$ , where  $\sigma$  and  $S$  are respectively the electrical conductivity and the Seebeck coefficient of the material, and  $T$  is the temperature. The higher  $ZT$ , the more efficient thermoelectric energy conversion will be, which is the key to making solid-state thermoelectric converters competitive with traditional electric generators or refrigerators. By looking at its expression, it is clear that reducing  $\kappa$  is an efficient way to enhance  $ZT$ .

Since, in semiconductors, heat is mostly transferred by phonons, these two contradictory demands can be satisfied by modifying phonon modes and interactions in an appropriate way. Enhancement can be achieved by reducing impurities or imperfections in the crystal, by isotopically purifying it, or by using new materials such as graphene [5,14].

Reduction can be obtained by alloying or by nanostructuring the thermoelectric semiconductor materials, since nanoparticles act as extrinsic phonon-scattering centers [3,13].

The theoretical study of thermal conductivity requires knowledge of crystal vibration spectra and of anharmonic forces, as well as of isotope effects, phonon interaction with the sample boundaries, crystal defects, etc. [15–17]. Steady state thermal conductivity has been understood for many decades. Typically, it is assumed that all the phonon scattering processes can be described by relaxation times that depend on the phonon frequency and temperature. Additionally, linear energy relations are assumed, neglecting dispersion.

At the lowest temperatures boundary scattering predominates and the phonon mean free path is comparable with the crystal dimensions, which causes the conductivity to increase as  $T^3$ . The maximum conductivity occurs at  $T \approx 0.05 \theta_D$ , where impurities are the dominant interaction,  $\theta_D$  being an averaged Debye temperature over all phonon branches. As temperature further increases, umklapp processes become prevalent, and the conductivity decreases as the inverse of  $T$ .

As clock speeds of modern microprocessors have increased, studies on short time scale energy transport have been recently prompted [2]. In fact, the current speed of microprocessors is in the order of gigahertz and is expected to reach 100 GHz in the near future. Thermal conductivity is frequency dependent, and dielectric and semiconductor materials are strongly insulating at frequencies of temperature disturbances near to or exceeding the phonon inverse mean relaxation time.

Finally, graphene has gained great attention due to the ease in isolating a single sheet of graphite and to its very good mechanical, thermal and electric properties [10,18]. In particular, graphene nanoribbons are potentially excellent thermoelectrics owing to their very high thermoelectric figure-of-merits [19].

The main aim of the present review paper, which is also its main novelty, is to recast the results about thermal conductivity obtained in [20–22] into a common framework suitable for describing energy transfer in both 3D and 2-D materials. The results shown for the materials taken into account examine the main thermal conductivity characteristics listed above and are in good qualitative and quantitative agreement with those found in the literature. We also underline that these results are relative to different values of temperature, dimensions and other physical characteristics of the materials with respect to those in [20–22]. The paper can be considered a natural continuation of a previous review paper [23] and together with it confirms that MEP is a reliable method for devising, in a systematic way, macroscopic models for semiconductor materials.

The paper is organized in the following way. In Section 2, we briefly introduce the kinetic description of phonon transport and the formulas of the steady-state and the dynamical thermal conductivity which can be derived from it. In Section 3, we present a hierarchy of hydrodynamic-like models for energy transport both in 3D and 2-D materials, whose closure can be obtained by means of MEP. In Section 4, we revisit the formula for the lattice thermal conductivity which can be retrieved from the hierarchy of models. In Section 5, we apply the formula to the study of silicon and germanium conductivity, and we analyse the conductivity reduction which can be obtained by embedding germanium nanoparticles into a  $\text{Si}_{0.7}\text{Ge}_{0.3}$  alloy crystal. Eventually, in Section 6, we study the case of bulk graphene and graphene nanoribbons, taking into account a scattering which has recently been considered for explaining the ultra-low thermal conductivity of 2-D phononic crystals. This scattering is related to the presence of undercoordinated atoms at the longitudinal edges of the nanoribbons.

## 2. Kinetic Model and Callaway Formula for the Thermal Conductivity

Energy transport in semiconductors is essentially due to the collective movement or excitations of atoms in a crystal, which can be described in terms of phonons: the quanta of lattice vibrations [24]. The number of normal modes of vibration of a crystal lattice is equal to three times the number  $\nu$  of atoms in the unit cell, which is the smallest repeating portion of a crystal lattice. If  $\nu = 1$  there are only three acoustic modes which produce

nearly in phase oscillations of neighbour atoms and have long wavelength. For  $\nu = 2$  three optical modes are also present, which produce nearly in anti-phase oscillations. In this paper we will not consider the case  $\nu > 2$ . Acoustic phonons give rise to sound in solids, while optical phonons are easily excited by light. The three acoustical and the three optical modes have different directions of polarization: there are, in fact, one longitudinal and two transversal oscillations, for both optical and acoustic modes, which are indicated as LA, TA, LO, TO respectively. In the semiclassical approximation, valid when relevant length/time scales on which the single-particle Green's function varies are much longer than coherence lengths and times [25], the state of a phonon in a given branch can be described by its wave vector  $\mathbf{q}$  and its polarization,  $\mathbf{q}$  varying in the first Brillouin zone  $B$  of the reciprocal lattice, which is the Fourier transform of the crystal lattice. For values of  $\mathbf{q}$  not far from 0, the dispersion relation, which relates the phonon energy  $\epsilon$  to the wave vector, is almost linear for the acoustic branches (Debye approximation), while it is almost flat for the optical branches (Einstein approximation):

$$\epsilon_{ac} \approx \hbar v_{ac} |\mathbf{q}|, \quad ac = LA, TA, \quad \epsilon_{op} \approx \text{const}, \quad op = LO, TO,$$

with  $\hbar$  the reduced Planck constant and  $v$  the modulus of the phonon group velocity  $\mathbf{v} := \frac{1}{\hbar} \nabla_{\mathbf{q}} \epsilon$ , which is constant for the acoustic phonons and negligible for the optical ones. Therefore, within a good approximation, energy transfer can be ascribed only to longitudinal and transverse acoustic phonons, which are the only ones we will take into account in the following.

At a kinetic level, the description [17] of phonon behavior can be done by using the phonon occupation number  $g_p(\mathbf{x}, t, \mathbf{q})$ , which depends on the space vector  $\mathbf{x}$ , the time  $t$ , the phonon wave vector and polarization  $p = LA, TA$ . The Boltzmann–Peierls equation governs the time evolution of  $g$ :

$$\frac{\partial g_p}{\partial t} + \mathbf{v}_p \cdot \nabla_{\mathbf{x}} g_p = C_p(g_p), \quad p = LA, TA, \quad (1)$$

where the collision operator  $C_p$ ,  $p = LA, TA$  describes the scattering mechanisms of phonons among themselves, with the boundaries of the crystal, as well as with lattice imperfections. As regards interaction among phonons, it is due to fact that the various monochromatic waves freely propagate through the crystal without interacting only in the harmonic approximation. Higher order terms of the lattice potential, due to atomic oscillations around equilibrium positions, are taken into account as various processes of decay and scattering among these waves. Three phonon processes can be classified into normal and umklapp ones. A normal process conserves energy and momentum, whereas an umklapp one only conserves energy [26].

The expression of the collision operator is rather complex and a simplification, due to Callaway [15] and based on a relaxation time approximation, is usually adopted in the device simulations. It reads:

$$C_p = -\frac{g_p - g_p^{(0)}}{\tau_p^R} - \frac{g_p - g_p^{(1)}}{\tau_p^N},$$

where the  $\tau_p^R$ 's are the relaxation times for the resistive processes, which include umklapp scatterings and interactions with boundaries and imperfections, and conserve energy but not momentum, while the  $\tau_p^N$ 's are the relaxation times for the normal processes, which, as said, conserve momentum too. The resistive scatterings make the phonon distribution converge to the Planckian one,

$$g_p^{(0)} = \left[ \exp\left(\frac{\epsilon_p}{k_B T}\right) - 1 \right]^{-1}, \quad p = LA, TA,$$

with  $k_B$  the Boltzmann constant and  $T$  the local temperature [27]. While  $g_p^{(1)}$  is the displaced Planck distribution to which, due to the normal processes,  $g_p$  tends to

$$g_p^{(1)} = \left[ \exp\left(\frac{\epsilon_p - \lambda_p \cdot \mathbf{q}}{k_B T}\right) - 1 \right]^{-1} \approx g_p^{(0)} + \frac{T}{\epsilon_p} \frac{dg_p^{(0)}}{dT} \lambda_p \cdot \mathbf{q}.$$

In [2,15], the following expression of  $\lambda_p$  is used:

$$\lambda_p = -\hbar \beta_p |\mathbf{v}_p|^2 \frac{\nabla_{\mathbf{x}} T}{T},$$

where there appear the applied temperature gradient and a parameter  $\beta_p$  (Callaway parameter), with the dimension of a relaxation time. The latter is found by requiring that the total phonon momentum production, for  $N$  processes, equals zero:

$$\int_{\mathbf{B}} \mathbf{q} \frac{g_p - g_p(\lambda_p)}{\tau_p^N} d\mathbf{q} = 0. \quad (2)$$

Following the procedure used by Callaway, Ezzahri and Joulain [2] have found a formula able to reproduce the key aspects of the dynamical thermal conduction by phonons and to give the steady-state conductivity as a particular case. They make the following hypotheses:

1.  $g_p$  depends on  $\mathbf{x}$  only through  $T$  so that  $\nabla_{\mathbf{x}} g_p = \frac{dg_p}{dT} \nabla_{\mathbf{x}} T$ ,
2.  $\frac{dg_p}{dT} \approx \frac{dg_p^{(0)}}{dT}$ .

Under these hypotheses (see [2] for details), Equation (1) becomes:

$$\tau_p^C \frac{\partial g_p}{\partial t} + g_p = g_p^{(0)} - \tau_p^{eff} \frac{dg_p^{(0)}}{dT} \mathbf{v}_p \cdot \nabla_{\mathbf{x}} T, \quad (3)$$

where

$$(\tau_p^C)^{-1} := (\tau_p^R)^{-1} + (\tau_p^N)^{-1}, \quad \tau_p^{eff} := \left(1 + \frac{\beta_p}{\tau_p^N}\right) \tau_p^C$$

are the combined total and the effective relaxation times, respectively. Equation (3) can be solved by Fourier transforming both sides, obtaining

$$\widehat{g}_p(\mathbf{x}, \Omega) = \frac{1}{1 - i\Omega\tau_p^C} \widehat{g}_p^{(0)} - \frac{\tau_p^{eff} \frac{dg_p^{(0)}}{dT}}{1 - i\Omega\tau_p^C} \mathbf{v}_p \cdot \widehat{\nabla_{\mathbf{x}} T}, \quad (4)$$

where the hat indicates the Fourier transform,  $i$  is the imaginary unit and  $\Omega$  is the circular frequency. Here, there is the additional hypothesis that  $\tau_p^C$ ,  $\tau_p^{eff}$  and  $\frac{dg_p^{(0)}}{dT}$ ,  $p = LA, TA$ , have negligible time dependence [2].

This solution can be used to compute the Fourier transform of the heat flux  $\widehat{\mathbf{Q}}$ , which reads:

$$\begin{aligned} \widehat{\mathbf{Q}} &:= \sum_p y_p \int_{\mathbf{B}} \epsilon_p \mathbf{v}_p \widehat{g}_p d\mathbf{q} = - \left[ \sum_p y_p \int \frac{\tau_p^{eff} \epsilon_p}{1 - i\Omega\tau_p^C} \mathbf{v}_p \otimes \mathbf{v}_p \frac{dg_p^{(0)}}{dT} d\mathbf{q} \right] \cdot \widehat{\nabla_{\mathbf{x}} T} \\ &= : -\kappa(\Omega) \widehat{\nabla_{\mathbf{x}} T}, \end{aligned}$$

from which the dynamical lattice thermal conductivity  $\kappa(\Omega)$  can be defined,  $y_{LA} = \frac{1}{(2\pi)^3}$ ,  $y_{TA} = \frac{2}{(2\pi)^3}$  being the longitudinal and transversal acoustic phonon density of states, and  $\otimes$  indicating the tensor product.

It is easy to see that the real and imaginary parts of the thermal conductivity respectively read:

$$\kappa_r(\Omega) = \sum_p \frac{4 \pi y_p k_B^4 T^3}{3 \hbar^3 v_p} \int_0^{\theta_p^D/T} \frac{\tau_p^{eff}(x)}{1 + (\Omega \tau_p^C(x))^2} \frac{x^4 e^x}{(e^x - 1)^2} dx, \tag{5}$$

$$\kappa_i(\Omega) = \sum_p \frac{4 \pi y_p k_B^4 T^3}{3 \hbar^3 v_p} \int_0^{\theta_p^D/T} \frac{\Omega \tau_p^C(x) \tau_p^{eff}(x)}{1 + (\Omega \tau_p^C(x))^2} \frac{x^4 e^x}{(e^x - 1)^2} dx, \tag{6}$$

where  $\theta_p^D$  is the Debye temperature [5] of the acoustic branch  $p = LA, TA$ , and  $x := \frac{\epsilon_{LA/TA}}{k_B T}$ . Eventually, by imposing (2), one finds:

$$\beta_p = \frac{\int_0^{\theta_p^D/T} \frac{\tau_p^C(x)}{\tau_p^N(x)} \frac{x^4 e^x}{(e^x - 1)^2} dx}{\int_0^{\theta_p^D/T} \frac{\tau_p^C(x)}{\tau_p^N(x) \tau_p^R(x)} \frac{x^4 e^x}{(e^x - 1)^2} dx}.$$

### 3. Macroscopic Models

In [20], by exploiting a hierarchy of hydrodynamic-like models, it has been derived a new formula for lattice conductivity, from which it is possible to find results comparable to those coming from (5) and (6).

These macroscopic models can be built by applying the moments method to the Boltzmann–Peierls Equation (1). In particular, the following weight functions of  $\mathbf{q}$  can be considered:

$$\{\psi_p(\mathbf{q})\} : = \{\epsilon_p, \epsilon_p^{\tilde{M}(1)} \mathbf{v}_p, \dots, \epsilon_p^{\tilde{M}(\tilde{M})} \mathbf{v}_p\},$$

where

$$\tilde{M} = \tilde{M}(M) := \begin{cases} \frac{M-1}{s_1}, & \text{if } M = 1, \dots, s_1 + 1, \\ 1 + \frac{M-1-s_1}{s_2}, & \text{if } M = s_1 + 2, \dots, \tilde{M}, \end{cases}$$

with  $s_1, s_2, \tilde{M} \in \mathbb{N}$  to be suitably fixed. The moments of  $g_p$  corresponding to the above-chosen weight functions are:

$$W_p = y_p \int_B \epsilon_p g_p d\mathbf{q},$$

$$\mathbf{Q}_p^M = y_p \int_B \epsilon_p^{\tilde{M}(M)} \mathbf{v}_p g_p d\mathbf{q}, \quad M = 1, \dots, \tilde{M}. \tag{7}$$

The state variables  $W_p, p = LA, TA$  are the phonon average energies, the  $\mathbf{Q}_p := \mathbf{Q}_p^{s_1+1}, p = LA, TA$  are the heat fluxes, while the other variables do not have an immediate physical meaning. Different moments can be chosen [20,28,29] according to the physical situation one wants to describe, which governs also the choice of  $s_1, s_2$  and  $\tilde{M}$ . Here, only the energies and vector moments are taken into account, since we are interested in thermal conductivity, and the results indicate that these moments are very appropriate to its study. By multiplying the Boltzmann–Peierls equation and integrating over the Brillouin zone, one can derive the evolution equations for the state variables (7):

$$\frac{\partial}{\partial t} \begin{pmatrix} W_p \\ \mathbf{Q}_p^M \end{pmatrix} + \nabla_{\mathbf{x}} \cdot \begin{pmatrix} \mathbf{Q}_p \\ \mathbf{T}_p^M \end{pmatrix} = \begin{pmatrix} C_{W_p} \\ C_{\mathbf{Q}_p^M} \end{pmatrix},$$

$$M = 1, \dots, \tilde{M}. \tag{8}$$

In the above-written equations, the following extra-fluxes and production terms are present:

$$\mathbf{T}_p^M = y_p \int_B \epsilon_p^{\tilde{M}(M)} \mathbf{v}_p \otimes \mathbf{v}_p g_p d\mathbf{q}, \quad M = 1, \dots, \bar{M}.$$

$$C_{W_p} = y_p \int_B \epsilon_p C_p(g_p) d\mathbf{q},$$

$$C_{\mathbf{Q}_p^M} = y_p \int_B \epsilon_p^{\tilde{M}(M)} \mathbf{v}_p C_p(g_p) d\mathbf{q}, \quad M = 1, \dots, \bar{M},$$

which are further unknowns. The variables  $\mathbf{T}_p^{s_1+1}$ ,  $C_{W_p}$  and  $C_{\mathbf{Q}_p^{s_1+1}}$ ,  $p = LA, TA$ , respectively are the fluxes of the energy fluxes, and the energy and energy flux productions, while the other extra-fluxes and production terms do not have an immediate physical meaning.

The number of the unknowns present in the evolution equations is greater than the number of the equations, therefore one needs constitutive equations for the extra-variables. A physically well sound method to get these constitutive equations is based on the exploitation of MEP [30–35]. This principle states that the occupation number can be approximated by that which maximizes the total entropy under the constraints that it reproduces the moments which have been chosen to describe the phonon state. If we neglect the mutual interactions, the phonon entropy can be written as

$$\mathcal{S} = -k_B \sum_p y_p \int_B \left[ g_p \ln g_p - (1 + g_p) \ln (1 + g_p) \right] d\mathbf{q}.$$

The solution of this constrained extremum problem is given by:

$$g_p^{ME} = \frac{1}{\exp(\epsilon_p \Lambda_{W_p} + \mathbf{v}_p \cdot \sum_M \epsilon_p^{\tilde{M}(M)} \Lambda_{\mathbf{Q}_p^M}) - 1}. \tag{9}$$

Under the same hypotheses as in [2,15], we suppose that the phonon system is not too far from local equilibrium, therefore linearizing (9) with respect to the vector variables, one gets:

$$g_p^{ME} \approx \frac{1}{\exp(\epsilon_p \Lambda_{W_p}) - 1} - \frac{\exp(\epsilon_p \Lambda_{W_p})}{(\exp(\epsilon_p \Lambda_{W_p}) - 1)^2} \mathbf{v}_p \cdot \sum_M \epsilon_p^{\tilde{M}(M)} \Lambda_{\mathbf{Q}_p^M}. \tag{10}$$

The Lagrange multipliers  $\Lambda$  are related to the state variables through the constraints (7). From the inversion of these relations, one can obtain occupation numbers which depend on  $(\mathbf{x}, t)$  only through the state variables, therefore the needed closure relations can be retrieved by substituting (10) into the integrals which define the extra-variables. It can also be noticed that (10) is closely associated to the Grad’s distribution which is extensively employed in extended thermodynamics [29,36,37].

*Closure*

Here, the inversion of the constraint relations (7) is performed, after substituting the approximate MEP occupation numbers, and the closure relations are found.

For usual semiconductors, both three-dimensional and two-dimensional, from the scalar constraints, the following expressions of the energy multipliers can be obtained:

$$\Lambda_{W_p} = d_p^{-1}(W_p),$$

where the  $d_p^{-1}$ ’s are the inverse of the functions:

$$d_p(\Lambda_{W_p}) := y_p \int_B \frac{\epsilon_p}{\exp(\epsilon_p \Lambda_{W_p}) - 1} d\mathbf{q},$$

which are invertible since  $d'_p(\Lambda_{W_p}) < 0$ , where the prime indicates the derivative of the function with respect to its argument.

Moreover, if the dispersion relations are invariant for rotations of  $\frac{\pi}{2}$  around any of the coordinate axes, one finds for the vector Lagrange multipliers:

$$\Lambda_{\mathbf{Q}_p^M} = \sum_K b_{MK}^p(W_p) \mathbf{Q}_p^K,$$

where the  $\bar{M} \times \bar{M}$  matrices  $\mathcal{B}^p := (b_{MK}^p)$  are the inverse of the matrices  $\mathcal{A}^p := (a_{MK}^p)$  of elements:

$$a_{MK}^p := -y_p \int_B |\mathbf{v}_p|^2 (n_1)^2 \frac{\epsilon_p^{\tilde{M}(M)+\tilde{M}(K)} \exp(\epsilon_p \Lambda_{W_p})}{(\exp(\epsilon_p \Lambda_{W_p}) - 1)^2} d\mathbf{q},$$

where  $n_1$  is the component along the  $x$  axis of  $\frac{\mathbf{q}}{|\mathbf{q}|}$ .

The above-written expressions of the Lagrange multipliers can be used to get the constitutive equations for the extra-variables. As regards the extra-fluxes, one has:

$$\mathbf{T}_p^M = \tilde{K}_M^p(T) \mathbf{I}_n,$$

with  $\mathbf{I}_n$  the identity tensor of rank equal to the dimensionality  $n$  of the material, and

$$\tilde{K}_M^p(T) = y_p \int_B |\mathbf{v}_p|^2 (n_1)^2 \frac{\epsilon_p^{\tilde{M}(M)}}{\exp(\epsilon_p \Lambda_{W_p}) - 1} d\mathbf{q}, \quad M = 1, \dots, \bar{M}.$$

In order to compute the production terms, it is necessary to get the asymptotic occupation numbers relative to the resistive processes and the normal ones, respectively. We remind that the approximate collision operator has the form:

$$-\frac{g_p^{ME} - g_p^{(0)}(\lambda_p)}{\tau_p^R(\epsilon_p)} - \frac{g_p^{ME} - g_p^{(1)}(\lambda_p, \lambda_p)}{\tau_p^N(\epsilon_p)},$$

where the unknowns  $\lambda_p$  and  $\lambda_p$  have to be determined in such a way to ensure the conservation of energy, and, as regards the normal scattering, also that of momentum. Exploiting the first requirement, one has

$$\begin{aligned} 0 &= \int_B \epsilon_p \frac{g_p^{ME} - g_p^{(0)}(\lambda_p)}{\tau_p^R(\epsilon_p)} d\mathbf{q} + \int_B \epsilon_p \frac{g_p^{ME} - g_p^{(0)}(\lambda_p)}{\tau_p^N(\epsilon_p)} d\mathbf{q} \\ &= \int_B \epsilon_p \frac{[\exp(\epsilon_p \Lambda_{W_p}) - 1]^{-1} - g_p^{(0)}(\lambda_p)}{\tau_p^R(\epsilon_p)} d\mathbf{q} \\ &+ \int_B \epsilon_p \frac{[\exp(\epsilon_p \Lambda_{W_p}) - 1]^{-1} - g_p^{(0)}(\lambda_p)}{\tau_p^N(\epsilon_p)} d\mathbf{q}, \end{aligned}$$

from which we find

$$\lambda_p = \Lambda_{W_p}.$$

Since, from extended thermodynamics [27,32], the relations between the acoustic phonon local temperature  $T$  and the Lagrange multipliers corresponding to their energies are given by:

$$\Lambda_{W_p} = 1/k_B T,$$

we can conclude that

$$\lambda_p = 1/k_B T.$$

After that, imposing condition (2), see [15], which in the present case reads:

$$C_{\mathbf{P}_p}^{(N)} = - \int \hbar \mathbf{q} / \tau_p^N \left[ - \frac{y_p \exp(\epsilon_p \Lambda_{W_p})}{(\exp(\epsilon_p \Lambda_{W_p}) - 1)^2} \mathbf{v}_p \cdot \sum_M \epsilon_p^{\tilde{M}(M)} \Lambda_{\mathbf{Q}_p^M} - \frac{y_p \exp(\epsilon_p \Lambda_{W_p})}{(\exp(\epsilon_p \Lambda_{W_p}) - 1)^2} \frac{\lambda_p \cdot \mathbf{q}}{k_B T} \right] d \mathbf{q} = 0,$$

with  $\mathbf{P}_p := y_p \int_B \hbar \mathbf{q} g_p d \mathbf{q}$ , the  $p$ -phonon momentum, and  $C_{\mathbf{P}_p}^{(N)} := -y_p \int_B \hbar \mathbf{q} \frac{g_p - g_p^{(1)}(\lambda_p)}{\tau_p^N} d \mathbf{q}$ , the part of its production resulting from normal scattering, we have

$$\lambda_p = -k_B T \sum_M \frac{\tilde{J}_M^{(p,N)}(\Lambda_{W_p})}{\tilde{J}^{(p,N)}(\Lambda_{W_p})} \Lambda_{\mathbf{Q}_p^M}, \quad p = LA, TA,$$

where

$$\tilde{J}^{(p,N)}(\Lambda_{W_p}) := \int_B |\mathbf{q}|^2 \frac{\exp(\epsilon_p \Lambda_{W_p})}{\tau_p^N (\exp(\epsilon_p \Lambda_{W_p}) - 1)^2} (n_1)^2 d \mathbf{q},$$

$$\tilde{J}_M^{(p,N)}(\Lambda_{W_p}) := \int_B |\mathbf{q}| |\mathbf{v}_p| \frac{\epsilon_p^{\tilde{M}(M)} \exp(\epsilon_p \Lambda_{W_p})}{\tau_p^N (\exp(\epsilon_p \Lambda_{W_p}) - 1)^2} (n_1)^2 d \mathbf{q},$$

having assumed that  $\mathbf{v}_p = |\mathbf{v}_p| \frac{\mathbf{q}}{|\mathbf{q}|}$ .

After that, it is possible to compute all the production terms relative to the phonon interactions that have been considered. They have the following form:

$$C_{W_p} = 0,$$

$$C_{\mathbf{Q}_p^M}^{(N)} = \sum_{K,\eta} c_{MK}^{p,\eta}(T) \mathbf{Q}_p^K, \quad p = LA, TA,$$

where the sum over  $K$  goes from 0 to  $\tilde{M}$  and that over  $\eta$  takes into account the specified scattering types. Eventually, the expressions of the coefficients  $c_{MK}^\eta$  depend, as we will see, on the phonon dispersion relations of the material taken into account and the relaxation times of phonon processes.

#### 4. A Formula for the Lattice Thermal Conductivity

In this section, exploiting the previously introduced hierarchy of hydrodynamical models, we show how it is possible to derive a formula for the steady-state and dynamical conductivity of semiconductors. Let's consider the evolution equations of the fluxes  $\mathbf{Q}_p^M$ ,  $M = 1, \dots, \tilde{M}$ , substituting in them the closure expressions, they read:

$$\frac{\partial}{\partial t} (\mathbf{Q}_p^M)_i + \tilde{K}_M^{p'}(T) \frac{\partial T}{\partial x_i} = \sum_{K,\eta} c_{MK}^{p,\eta}(T) (\mathbf{Q}_p^K)_i, \quad i = 1, \dots, n, \quad M = 1, \dots, \tilde{M}. \quad (11)$$

It is worth noticing that the equation for the heat flux ( $M = s_1 + 1$ ) is Cattaneo's equation, and for this reason it is possible to consider the hierarchy of models as generalizing this equation. Assuming, as in [2], that the time variation of the  $\tilde{K}_M^{p'}$ , and  $C^p := \sum_\eta (c_{MK}^{p,\eta})$ ,  $p = LA, TA$ ,  $M, K = 1, \dots, \tilde{M}$ , is negligible, making the Fourier transform of (11) and solving the resulting system with respect to the Fourier transform of the fluxes, one gets

$$\widehat{(\mathbf{Q}_p^M)}_i = \sum_L (C^p + i\Omega \mathcal{I}_M)_{ML}^{-1} \tilde{K}_L^{p'}(T) \frac{\partial \widehat{T}}{\partial x_i}, \quad i = 1, \dots, n,$$

with  $\mathcal{I}_{\bar{M}}$  the identity tensor of rank  $\bar{M}$ . For  $M = s_1 + 1$ , we have the relation between the Fourier transforms of the heat flux and of the temperature gradient, from which the following expression for the dynamical thermal conductivity is retrieved:

$$\begin{aligned}\kappa(\Omega) &= - \sum_{p,M} \left( i\Omega \mathcal{I}_{\bar{M}} + \mathcal{C}^p(T) \right)_{1M}^{-1} \tilde{K}'_M{}^p(T) \\ &= - \sum_{p,L,M} (\Omega^2 \mathcal{I}_{\bar{M}} + (\mathcal{C}^p)^2)_{1L}^{-1} (\mathcal{C}^p)_{LM} \tilde{K}'_M{}^p + i\Omega \sum_{p,M} (\Omega^2 \mathcal{I}_{\bar{M}} + (\mathcal{C}^p)^2)_{1M}^{-1} \tilde{K}'_M{}^p.\end{aligned}\quad (12)$$

In the previous expression the real and imaginary parts of  $\kappa(\Omega)$  are the Hilbert transforms of one other, which implies the fulfillment of the causality requirement: the temperature gradient and the heat flux are the cause and the effect, respectively [2].

Taking  $\Omega = 0$  in (12), one obtains the steady-state thermal conductivity, and it is worth noticing that it is the same one would get by applying the Maxwellian iteration procedure to Equation (8). At the first order, one has to introduce the equilibrium moments in the left-hand sides of (11), obtaining in such a way a relation between the fluxes and the temperature gradient. The Maxwell iteration has been employed, e.g., to get the viscosity and thermal conductivity of gases [29,37]. In addition, we wish to point out that the result for the thermal conductivity would not be affected by using further scalar moments and/or tensor moments of higher order.

Let us analyse the condition according which the variation in time of the temperature is much slower than that of the fluxes [2]. Let us rescale the variables, by introducing a characteristic time  $\bar{t}$ , temperature  $\bar{T}$ , length  $\bar{l}$  and collisional frequency  $\bar{\nu}_c$ :

$$T = \bar{T} \tilde{T}, \quad \mathbf{Q}^M = (k_B \bar{T})^{M-1} \frac{\kappa \bar{T}}{\bar{l}} \tilde{\mathbf{Q}}^M, \quad \mathbf{x} = \bar{l} \tilde{\mathbf{x}}, \quad t = \bar{t} \tilde{t}.$$

From Equations (8) and (11), one can deduce:

$$\begin{aligned}\frac{\partial \tilde{T}}{\partial \tilde{t}} &\propto - \frac{\kappa \bar{T}}{c_V \bar{l}^2}, \\ \frac{\partial \tilde{\mathbf{Q}}^M}{\partial \tilde{t}} &\propto - \bar{\nu}_c \tilde{\mathbf{Q}}^M, \text{ or greater in magnitude,}\end{aligned}$$

with  $c_V = \frac{dW}{dT}$  the material's heat capacity. From a comparison of the last two expressions, it is possible to deduce that, if the condition

$$\bar{l} \gg \left( \frac{\kappa}{c_V \bar{\nu}_c} \right)^{\frac{1}{2}}$$

is satisfied, then the assumption is valid, which means that the distance over which the temperature changes has to be large enough. e.g., in the case of Si, over a temperature range 200–800 K,  $\left( \frac{\kappa}{c_V \bar{\nu}_c} \right)^{\frac{1}{2}}$  is at most of the order of tenths of microns.

### 5. Three-Dimensional Materials

In the case of three-dimensional materials, in addition to take linear dispersion relations for the acoustic phonon microscopic energy, in the literature the first Brillouin zone is usually approximated with a sphere. This is commonly done to obtain the values of the physical parameters present in the relaxation times. For example, the effective sample diameter and the Grüneisen constants, which appear in the relaxation times of the normal and boundary processes respectively, are obtained by taking a fitting of the experimental data for the steady-state thermal conductivity [5]. If one would use different dispersion relations, new fittings would be required. Nonetheless, the model can deal with generic dispersion

relations (see e.g., [16,38] and the case of graphene in Section 6), the only disadvantage being more complicated integral expressions for closure relations.

In the following, we report the relaxation times of the main phonon scattering mechanisms present in 3D materials. For the normal scattering processes, one has [5]:

$$[\tau_{LA}^N]^{-1} = B_{LA}^N \left(\frac{k_B}{\hbar}\right)^2 x^2 T^5, \quad B_{LA}^N = \frac{k_B^3 \gamma_{LA}^2 V}{M \hbar^2 v_{LA}^5},$$

$$[\tau_{TA}^N]^{-1} = B_{TA}^N \frac{k_B}{\hbar} x T^5, \quad B_{TA}^N = \frac{k_B^4 \gamma_{TA}^2 V}{M \hbar^3 v_{TA}^5},$$

where the  $\gamma$ 's are the Grünesen constants,  $V$  is the volume per atom, and  $M$  is the average mass of an atom in a crystal. The inverse resistive relaxation time is given by the sum of the boundary, umklapp, and impurity inverse relaxation times, which conserve only energy. They respectively read:

$$[\tau_p^U]^{-1} = B_p^U \left(\frac{k_B}{\hbar}\right)^2 x^2 T^3 \exp(-\theta_p^D/3T), \quad B_p^U = \frac{\hbar \gamma_p^2}{M v_p^2 \theta_p^D}, \quad p = LA, TA,$$

$$[\tau_p^B]^{-1} = \frac{v_p}{d}, \quad p = LA, TA,$$

$d$  being the effective diameter of the sample,

$$[\tau_p^I]^{-1} = \frac{V k_B^4 \Gamma}{4\pi \hbar^4 v_p^3} x^4 T^4, \quad p = LA, TA.$$

If, as impurities, we consider the several naturally occurring isotopes which make up a single element, the mass-fluctuation phonon scattering parameter  $\Gamma$  reads:

$$\Gamma = \sum_i c_i \left[ \frac{m_i - M}{M} \right]^2, \quad M = \sum_i c_i m_i,$$

with  $m_i$  the atomic mass of the  $i$ th isotope and  $c_i$  its fractional atomic natural abundance.

As regards the functions appearing in the inversion and closure relations, one has:

$$d_p(\Lambda_{W_p}) = \frac{4\pi y_p}{\hbar^3 v_p^3 \Lambda_{W_p}^4} K_3^p(\Lambda_{W_p}),$$

with

$$K_\alpha^p(\Lambda_{W_p}) := \int_0^{\Lambda_{W_p} k_B \theta_p^D} \frac{x^\alpha}{e^x - 1} dx, \quad \alpha \in \mathbb{Q}^+,$$

$$a_{MK}^p(T) := -\frac{4}{3} \pi y_p \frac{(k_B T)^{\tilde{M}(K)+\tilde{M}(M)+3}}{(\hbar^3 v_p)} J_{\tilde{M}(M)+\tilde{K}(K)+2}^p$$

with

$$J_\alpha^p(T) := \int_0^{\theta_p^D/T} \frac{x^\alpha e^x}{(e^x - 1)^2} dx.$$

$$\tilde{K}_M^p = \frac{4}{3} \pi y_p \frac{(k_B T)^{\tilde{M}(M)+3}}{(\hbar^3 v_p)} K_{\tilde{M}(M)+2}^p(T),$$

$$c_{ML}^{(p,\eta)} = \sum_K q_{MK}^{(p,\eta)} b_{KL}^p, p = LA, TA,$$

where  $\eta = U, N, B, I$  respectively labels the umklapp, normal, boundary, and imperfections, and

$$q_{MK}^{(p,N)}(T) = \frac{4\pi y_p}{3\hbar^3 v_p} (k_B T)^{\tilde{M}(M)+\tilde{M}(K)+3} \left[ J_{\tilde{M}(M)+\tilde{M}(K)+2}^{(p,N)} - \frac{J_{\tilde{M}(M)+3}^{(p,N)} J_{\tilde{M}(K)+3}^{(p,N)}}{J_4^{(p,N)}} \right],$$

$$q_{MK}^{(p,\eta)}(T) = \frac{4\pi y_p}{3\hbar^3 v_p} (k_B T)^{\tilde{M}(M)+\tilde{M}(K)+3} J_{\tilde{M}(M)+\tilde{M}(K)+2}^{(p,\eta)} \quad \eta = U, B, I,$$

with

$$J_\alpha^{(p,\eta)}(T) := \int_0^{\theta_p^D/T} \frac{x^\alpha e^x}{\tau_p^\eta(x)(e^x - 1)^2} dx.$$

### 5.1. Application to Si and Ge

In this subsection we investigate the thermal conductivity of Si and Ge, which are two of the most used materials in semiconductor devices. The values of the physical parameters present in the formulas, are reported in Tables 1 and 2 for the cases of Si and Ge respectively, see, for example, [5]. We underline that no other parameter is used here and in the following.

**Table 1.** Physical parameters for Si.

Parameter	Value	Parameter	Value
$v_L$	8430 m/s	$\theta_L^D$	586 K
$v_T$	5840 m/s	$\theta_T^D$	240 K
$\gamma_L$	1.1	M	$4.66 \times 10^{-26}$ Kg
$\gamma_T$	0.6	V	$2 \times 10^{-29}$ m <sup>3</sup>
$d$	$4 \times 10^{-3}$ m	$\Gamma$	$2 \times 10^{-4}$

**Table 2.** Physical parameters for Ge.

Parameter	Value	Parameter	Value
$v_L$	4920 m/s	$\theta_L^D$	333 K
$v_T$	3540 m/s	$\theta_T^D$	150 K
$\gamma_L$	1.1	M	$12.6 \times 10^{-26}$ Kg
$\gamma_T$	0.6	V	$2.27 \times 10^{-29}$ m <sup>3</sup>
$d$	$4 \times 10^{-3}$ m	$\Gamma$	$6.08 \times 10^{-4}$

For the case of Si, in the interaction with impurities we have taken into account that silicon consists of three isotopes: <sup>28</sup>Si, <sup>29</sup>Si, and <sup>30</sup>Si, with concentrations 92.2%, 4.7%, and 3.1% respectively. While, the natural composition of germanium is the following: 20.5% <sup>70</sup>Ge, 27.4% <sup>72</sup>Ge, 7.8% <sup>73</sup>Ge, 36.5% <sup>74</sup>Ge and 7.8% <sup>76</sup>Ge.

The behavior of Si and Ge thermal conductivity is shown in Figure 1, where a comparison is made with the results of Morelli, Heremans and Slack in [5], found by means of (5) with  $\Omega = 0$ .

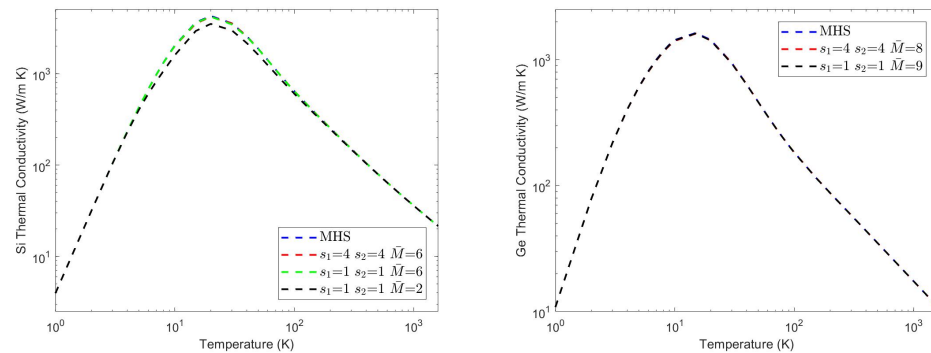


**Figure 1.** (Left): Silicon steady-state thermal conductivity vs. temperature. (Right): Germanium steady-state thermal conductivity vs temperature.

One can notice that by using eight vector moments the agreement is excellent in all the range of temperatures; however, out of the range  $[0, 200]$  K only two moments are already good. This is probably due to the fact that in the region  $[0, 200]$  K the phonon interaction with impurities is dominant, and its inverse relaxation time goes as  $\epsilon^4$ , therefore more vector moments are required for a correct description. We also underline that the use of weight functions with fractional powers of the energy is advantageous since the matrices  $i\Omega\mathcal{I} + \mathcal{C}$  and  $\Omega^2\mathcal{I} + \mathcal{C}^2$ , which have to be inverted are better conditioned.

In Figure 2 it can be seen that the conductivity can noticeably be increased by isotopically purifying the semiconductors. For example, the increase is around 13% and 29% respectively for silicon and germanium at room temperature. Moreover, the maximum conductivity is reached at slightly higher temperatures.

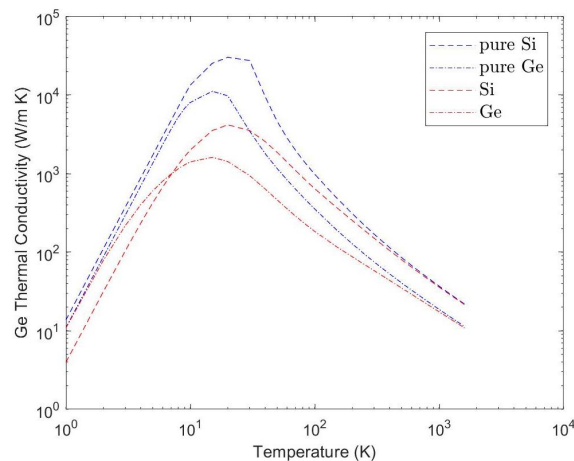


**Figure 2.** Pure silicon and germanium conductivities vs. temperature.

We also examine the dynamical conductivity, which is the behavior of the phonon gas in a bulk semiconductor when there is a dynamical temperature gradient due to an external disturbance. In Figure 3 the real and imaginary parts of Si and Ge thermal conductivities are represented in the frequency interval that goes from  $10^{-1}$  Hz to 160 THz, while in Figure 4 the amplitude and the phase are reported, the former, for low frequencies, being essentially equal to the real part. In qualitative agreement with [2], the amplitude has a constant value at low frequencies and starts rapidly diminishing at higher frequencies where the contribution of the imaginary part becomes relevant. Typically, this is a behavior of a first order low-pass thermal filter, which is caused by the fact that when the disturbance frequency becomes very high, the phonon gas is unable to follow it and the material acts as an insulator. The imaginary part has a Lorentzian shape, and the resonance frequency is equal to about  $1 \times 10^{10}$  Hz for both materials, corresponding to the order of the phonon mean relaxation time (10–100 ps).

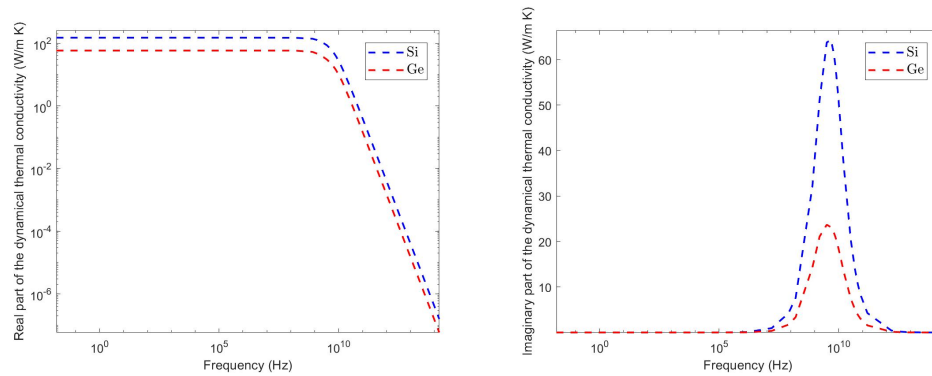


**Figure 3.** (Left): Real part of the dynamical thermal conductivity vs. frequency  $f$ . (Right): Imaginary part of the dynamical thermal conductivity vs.  $f$ .  $T = 300$  K.

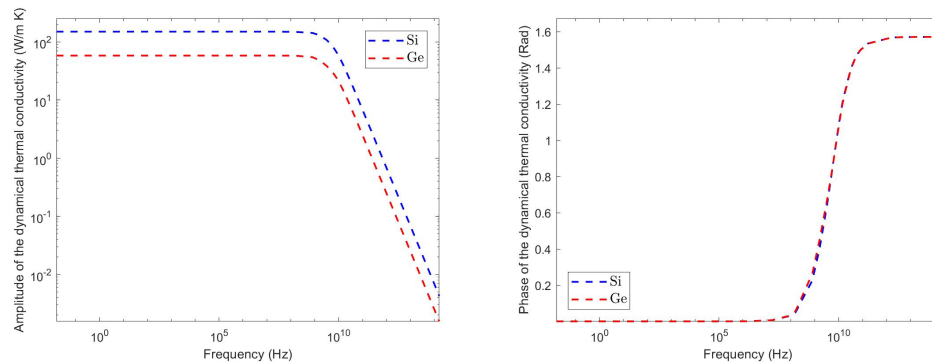


**Figure 4.** (Left): Amplitude of the dynamical thermal conductivity vs. frequency. (Right): Phase of the dynamical thermal conductivity vs. frequency.  $T = 300$  K.

Relatively to the phase, which can be seen in Figure 4 (right), it starts increasing at higher frequencies and grows to saturation at the value of  $\frac{\pi}{2}$ , faster at lower temperatures. This phase behavior describes the typical delay between the cause, which is the thermal disturbance, and the effect, which is represented by the heat flux. In Figure 5, the behavior of the amplitude (left) and the phase (right) of the silicon thermal conductivity are reported versus the frequency, at the temperatures  $T = 10, 100, 300, 600$  and  $1000$  K. It can be seen that at very high frequencies, above  $10^{11}$  Hz, the amplitude grows with  $T$ , but the rise slows down. Further, the amplitude goes as  $1/f$  in relation to frequency [8], for values greater than the cut-off frequency  $f_c$ , which is the point at which the amplitude reaches  $1/\sqrt{2}$  times its maximum value. At  $T = 300$  K,  $f_c \approx 3.3 \times 10^9$  Hz and it rises with  $T$ , however, at a temperature as high as  $T = 600$  K, the cut-off frequency is still less than 90 GHz, a value which will be soon reached by high-frequency microelectronic devices according to the International Technology Roadmap for Semiconductors. On the basis of these results, it is clear that understanding the dynamical behavior of the thermal conductivity is fundamental in controlling heat transport in microelectronic devices. In Figure 6, we report analogous results for Ge. The qualitative agreement with the results in [2] is good.

A comparison can be made also with the results in [8], which are obtained by using the molecular dynamics (MD) technique. In Figure 7 the trend of the amplitude of Si dynamical thermal conductivity is reported for frequencies from 10 GHz to 1 THz at the two values  $T = 200, 500$  K. There is a good agreement with Figure 1 in [8]: both figures show that the amplitude decreases of two orders of magnitude with respect to the reference bulk value of 150 W/mK. The asymptotic behavior of the amplitude, for  $\Omega \gg 2\pi f_c$ , can also be retrieved from (12):

$$|\kappa(\Omega)| \approx \sum_p \Omega^{-1} \tilde{K}_1^p(T), \quad \Omega \gg 2\pi f_c. \quad (13)$$

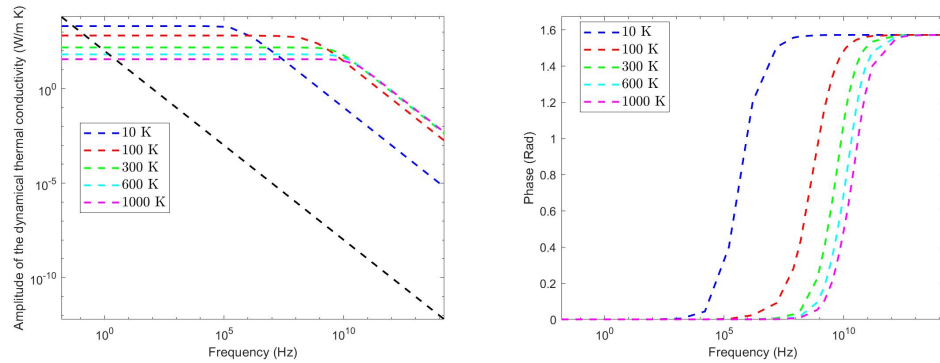


**Figure 5.** Amplitude (left) and phase (right) of the Si dynamical thermal conductivity vs. temperature. The black line behaves like  $1/f$ .

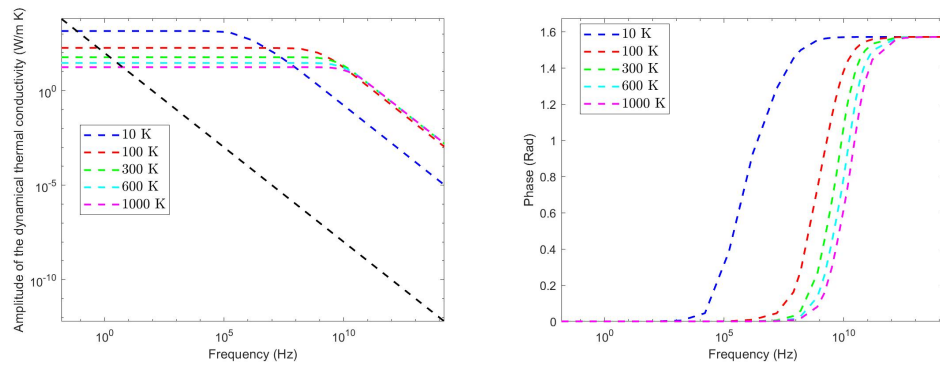


**Figure 6.** Amplitude (left) and phase (right) of the Ge dynamical thermal conductivity vs. temperature. The black line behaves like  $1/f$ .

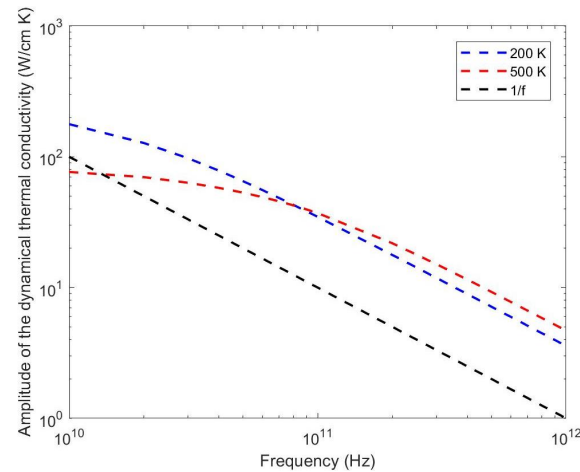


**Figure 7.** Amplitude of Si thermal conductivity for  $f$  going from 10 GHz to 1 THz at  $T = 200$  K and  $T = 500$  K.

It is worth noticing that the previous formula is independent of the choice of number of vector moments and predicts that the asymptotic amplitude drops as  $1/\Omega$ , which agrees both with Formula (6) of [8] and with the fitting of the molecular dynamics data in Figure 1 of [8]. We conclude this section by underlining that the right-hand side of (13) is independent of the phonon relaxation time, in agreement with the fact that ballistic transfer of phonons is predominant when  $\Omega \gg 2\pi f_C$  [8].

### 5.2. Application to $\text{Si}_{0.7}\text{Ge}_{0.3}$

In this subsection, we show how Formula (12) can also be applied to the embedding of spherical Ge nanoparticles of density  $\rho_{\text{Ge}} = 5323 \text{ Kg/m}^3$  in a  $\text{Si}_{0.7}\text{Ge}_{0.3}$  matrix. Inserting nanoparticles in a matrix is a challenging task, see e.g., [39,40] and references therein. To accomplish this, the particles have to be grown into the matrix without causing dislocations or defects, in addition the electron mean free path, unlike the phonon one, must not be shortened considerably. Recently, a wide range of materials have become available for incorporation in SiGe [40]. This is particularly important, since SiGe is excellent for integrating thermoelectrics into silicon technology, without increasing the cost of module production substantially. Suitable materials include silicides, germanides as well as Si and Ge themselves [2,39,40]. The type of nanoparticles is only one element of the problem, another is to determine the sizes and concentrations of the nanoparticles to achieve optimum efficiency, which is  $ZT$  above 0.5 at room temperature and  $ZT$  over 1 at higher temperatures.

In the linear regime, for the scattering with nanoparticles, if their shape is assumed to be spherical and a Matthiessen type interpolation between the long and the short wavelength scattering regimes is used, the inverse relaxation time is given by [2,40]:

$$\frac{1}{\tau_p^{np}} = \frac{v_p (\sigma_{pS}^{-1} + \sigma_{pL}^{-1})^{-1}}{V_{np}} f_{np}, \quad (14)$$

where  $V_{np} = \frac{4}{3}\pi R^3$  is the volume of a nanoparticle of radius  $R$ , and  $\sigma_{pS}$  and  $\sigma_{pL}$  are the short and long wavelength cross sections, which respectively read:

$$\sigma_{pS} = 2\pi R^2, \quad \sigma_{pL} = \frac{4\pi}{9} \left( \frac{\rho - \rho_{np}}{\rho} \right)^2 R^6 \left( \frac{\epsilon_p}{\hbar v_p} \right)^4,$$

$\rho$  being the density of the host matrix material,  $\rho_{np}$  that of the embedded nanoparticles, and  $f_{np}$  the nanoparticle volume fraction. The contribution stemming from the difference in elastic constants is disregarded.

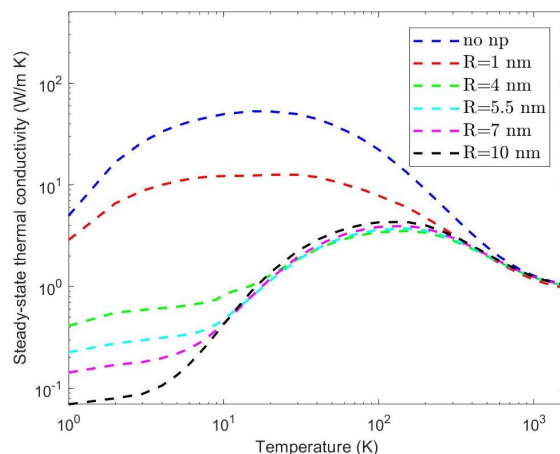
When the volume fraction of nanoparticles is up to 10% and their radius is in the range of 1 to 100 nm, nanoparticle influence on the electron mobility is small, which is crucial to achieving high figures of merit. The reason is that the electron mean free path (MFP) related to the interaction with nanoparticles is much longer than the intrinsic MFP due to the pure inelastic alloy scattering [3,40]. Moreover, nanoparticles, with the above-specified characteristics, do not have an effect on the intrinsic physical parameters of the semiconductor host alloy, which can be found in Table 3.

**Table 3.** Physical parameters for  $\text{Si}_{0.7}\text{Ge}_{0.3}$ .

$v_L$	6812 m/s	$\theta_L^D$	510 K
$v_T$	4769 m/s	$\theta_T^D$	213 K
$\gamma_L$	1	M	$6.9 \times 10^{-26} \text{ Kg}$
$\gamma_T$	0.7	V	$2.07 \times 10^{-29} \text{ m}^3$
$d$	$5 \times 10^{-3} \text{ m}$	$\Gamma$	0.2403
$\rho$	$3332 \text{ kg/m}^3$		

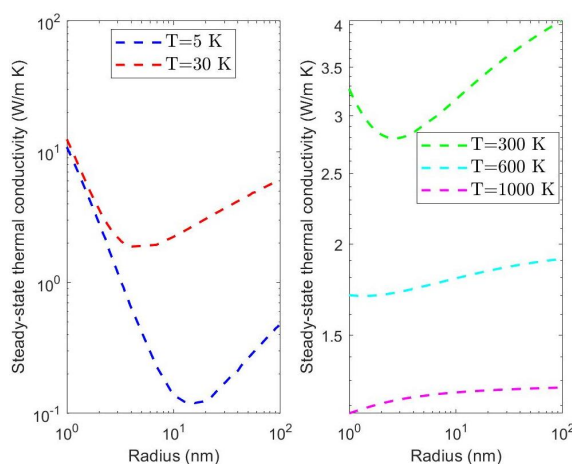
In Figure 8 it is represented the temperature behavior of the steady-state thermal conductivity  $\kappa(0)$ , for a nanoparticle fraction  $f_{np} = 2\%$ , and for some values of the nanoparticle radius. It is compared with the case when no nanoparticles are embedded. It can be seen that with increasing values of  $R$ , the thermal conductivity decreases and its peak shifts in the right direction, from  $T = 15 \text{ K}$  to  $T = 150 \text{ K}$  as the radius goes to 10 nm. The decrease is more pronounced at low temperatures [3], where the conductivity declines up to more than one order of magnitude as  $R$  reaches 10 nm, while it tends to saturation at high

temperatures of around 600 K. Moreover, differently from the case without nanoparticles, at low temperatures,  $\kappa(0)$  does not obey the  $T^3$  power law followed by the specific heat.



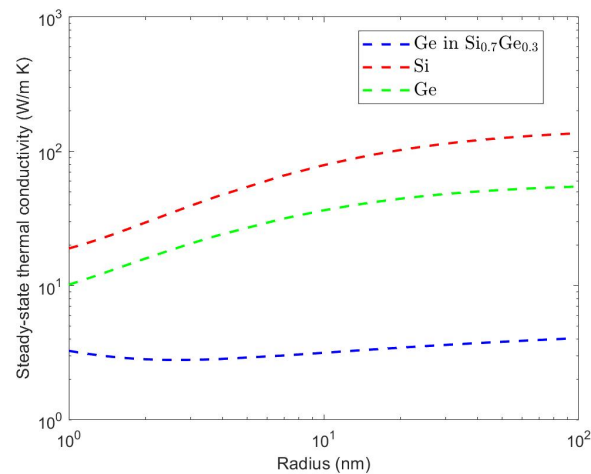
**Figure 8.** Steady-state thermal conductivity versus temperature, for  $f_{np} = 2\%$  and various values of the nanoparticle radius, no np labels the case in which there are no nanoparticles.

Figure 9 shows the steady-state thermal conductivity dependence on the nanoparticle radius for  $T = 5, 30, 300, 600, 1000$  K. There exists at every  $T$  a value  $R_{min}$  of  $R$  where the thermal conductivity reaches its minimum, and  $R_{min}$  becomes smaller as  $T$  increases, going from 15 nm at  $T = 5$  K to 1.3 nm at  $T = 600$  K (for  $T = 1000$  K it is below the range of values of  $R$  taken into account). This is a feature that has been already described in [3,40], and is ascribable to the interplay between the long and short wavelength scattering regimes, shown in Equation (14). From Figure 9, it can also be seen that, at higher temperatures, the presence of nanoparticles is less effective on conductivity, and, additionally, that the minimum is very broad, which is very advantageous from a manufacturing perspective, since it is not essential to have an extremely accurate control of the nanoparticle size.



**Figure 9.** Steady-state thermal conductivity versus  $R$ , for  $f_{np} = 2\%$  and  $T = 5, 30, 300, 600, 1000$  K.

In Figure 10 it is shown that the effect of embedding nanoparticles into a pure Si matrix (the same is true for Ge) is much less marked. A minimum is still reached in correspondence with an optimal size, but it has a higher value and is much narrower too. Nanoparticles are much more effective in alloys as in this case most of the heat is carried by the low frequency phonons [40], having a MFP longer than nanoparticle spacing, which makes these phonons most powerfully scattered by the nanoparticles embedded in the matrix.



**Figure 10.** Steady-state thermal conductivity versus  $R$  for nanocomposites with 0.2% volume fraction of Ge in Si, in Ge and in  $\text{Si}_{0.7}\text{Ge}_{0.3}$ , respectively, at  $T = 300$  K.

From Figure 11 (left), it is evident that the thermal conductivity diminishes as the fraction of nanoparticles increases, for example the maximum conductivity diminishes from 4.6 W/mK for  $f_{np} = 1\%$  to 1.78 W/mK for  $f_{np} = 10\%$ . This effect is confirmed also in the right side of the Figure, where it is shown the minimum conductivity as a function of temperature for various values of the nanoparticle volume fraction. The optimal conductivity is significantly lower than the alloy conductivity without nanoparticles, e.g., of around 67% at room temperature for  $f_{np} = 10\%$ .

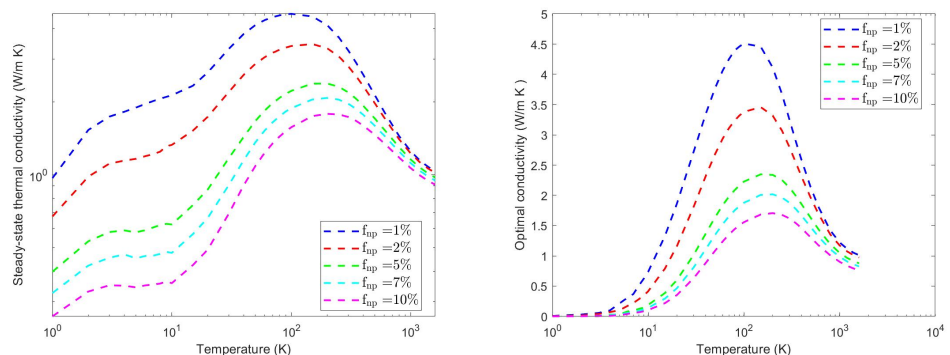


**Figure 11. (Left):** Steady-state thermal conductivity versus  $T$  for various values of the fraction of nanoparticles with radius  $R = 3$  nm in  $\text{Si}_{0.7}\text{Ge}_{0.3}$ . **(Right):** Minimum steady-state thermal conductivity versus  $T$  for various volume fractions of nanoparticles.

Eventually one finds that, even though the optimal value corresponds to different values of  $R$ , the value of  $R_{min}$  has a small variation when the temperatures goes from 200 K to 300 K, see Figure 12.

Regarding the dynamical thermal conductivity, the values  $T = 5$  K and  $T = 300$  K of the temperature are taken into account. For each case, see Figure 13, we examine how the amplitude of the dynamical conductivity changes with frequency  $f$ , for  $R = 1, 4, 8$  nm.

Compared to the case without nanoparticles, the main difference is that the alloy behavior is more similar to that of a second order low-pass thermal filter than a first order one [3]. The change of  $R$  has effects only up to medium frequencies and the asymptotic behavior goes as  $1/f$ , with the curves relative to different values of  $R$  which tend to superimpose at a frequency regime which becomes higher at higher temperatures. It can be noted that once again the dependence on  $R$  is smaller at room temperature.

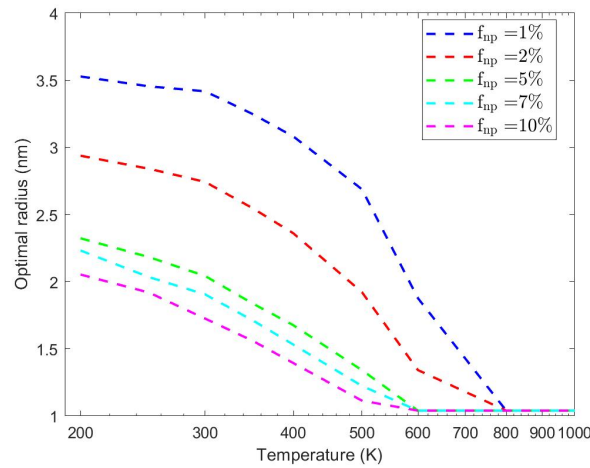


Figure 12. Optimal radius versus  $T$  for various volume fractions of nanoparticles in  $\text{Si}_{0.7}\text{Ge}_{0.3}$ .

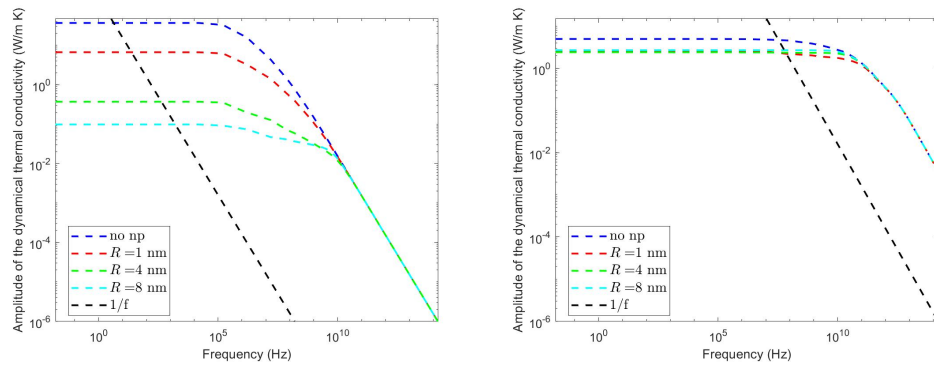


Figure 13. Amplitude of the dynamical thermal conductivity versus  $f$ , for  $f_{np} = 4\%$ . (Left):  $T = 5$  K. (Right):  $T = 300$  K. The black continuous–dotted lines behave like  $1/f$ .

In addition, the cut-off frequency  $f_c$  is greater in the case of inserted nanoparticles, as can be seen in Figure 14, where its behavior with respect to  $R$  is reported, for  $T = 20, 50, 100, 300, 500$  K. At low temperatures ( $T < 300$  K), initially  $f_c$  increases slowly with  $R$ , then there is a range of  $R$  with a steep slope, and finally  $f_c$  starts declining gradually. This kind of behavior, which is more evident at lower values of  $T$ , can also be attributed to the interplay between the long and short wavelength scattering regimes [3]. It can be seen that up to temperatures of 100 K in the steep slope range a change of a few nanometers in  $R$  leads to a variation in  $f_c$  of up to three orders of magnitude. However, for greater values of  $T$ ,  $f_c$  becomes less sensitive to  $R$ , due to the fact that in the high temperature regime the anharmonic process is the dominant phonon interaction.

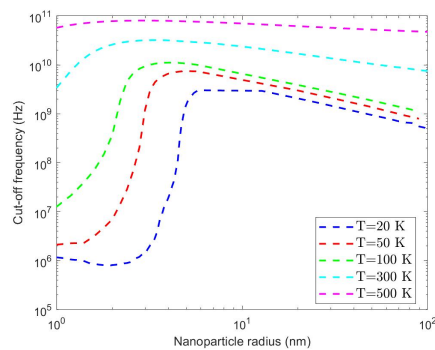


Figure 14. Cutoff frequency versus  $R$ ,  $f_{np} = 2\%$ .

### 6. Application to 2-D Materials: Graphene

In this section, the formula for the thermal conductivity is applied to suspended graphene nanoribbons. Graphene [9,18,41–52] is one of the most promising materials for future applications in nano-electronic devices, since its mechanical properties are very good and has an excellent electricity and heat conductivity. Particularly, this latter is very high [19,53] because of its peculiar lattice structure, which makes it an adequate prospect as a thermal management material in future nanoelectronic circuits [14].

Graphene is a two-dimensional hexagonally arranged lattice of carbon atoms, and it is a semimetal with no energy gap. Graphene nanoribbons (GNRs) are thin strips of graphene with variable width ( $y$ -direction) and length ( $x$ -direction), and with different roughness at their edges, see Figure 15.

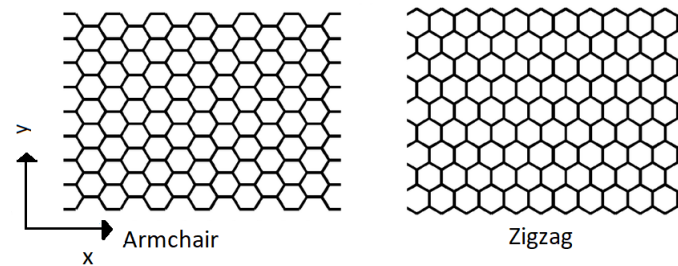


Figure 15. Armchair and zigzag graphene nanoribbons.

Phonon transport in GNRs can be modified by changing their dimensions, since width impacts the line-edge-roughness scattering, while an increase in length induces a crossover from ballistic to diffusive heat transport. In GNRs thermal flow can also be adjusted by modifying the isotope concentration, substrate [54], and ribbon crystal orientation. For the energy dispersion relations, we make use of the full ones, which can be obtained by means of the empirical dynamical matrix method consisting of the solution of the below-written eigenvalue problem

$$\mathcal{D}(\mathbf{q})\mathbf{u}(\mathbf{q}) = 0,$$

where  $\mathbf{u}(\mathbf{q}) = (\mathbf{u}_1(\mathbf{q}), \mathbf{u}_2(\mathbf{q}))^T$ , with  $T$ =transposed,  $\mathbf{u}_1(\mathbf{q}), \mathbf{u}_2(\mathbf{q})$  are the Fourier transforms of the displacement vectors of the two carbon atoms (A and B in Figure 16) contained in the unit cell, and

$$\mathcal{D} = \begin{pmatrix} \mathcal{D}^{(11)} & \mathcal{D}^{(12)} \\ \mathcal{D}^{(21)} & \mathcal{D}^{(22)} \end{pmatrix},$$

is the dynamical matrix given by:

$$\mathcal{D}^{(ij)} = \left( \sum_{j''} K^{ij''} - M_i \omega^2(\mathbf{q}) \right) \delta_{ij} - \sum_{j'} K^{ij'} e^{i\mathbf{q} \cdot \Delta \mathbf{R}_{ij'}},$$

$\delta_{ij}$  being the Kronecker delta,  $i, j = 1, 2$  labelling A and B. The index  $j''$  is summed over the nearest neighbours of the  $i$ -th atom, while  $j'$  is summed over the sites equivalent to the  $j$ -th atom, that is those differing from it by a lattice vector.  $\Delta \mathbf{R}_{ij}$  represents the relative position of the  $i$ -th atom with respect to the  $j$ -th atom, and the  $K$ 's are the three by three force constant tensors taking into account the binding forces between carbon atoms, whose construction is shown in [55]. One has:

$$K^{i,i_n} = \begin{pmatrix} \Phi_r^n & 0 & 0 \\ 0 & \Phi_{ti}^n & 0 \\ 0 & \vdots & \Phi_{to'}^n \end{pmatrix}$$

where  $i_n$  indicates the  $n$ th nearest neighbour of atom  $i$ , and  $r$ ,  $ti$  and  $to$  to respectively label the radial, transverse in-plane and transverse out-of-plane components of the force constants  $\Phi$ , which can be found in Table 4 [4].

**Table 4.** Force constants for graphene in units of 10 N/m.

Radial	In-Plane	Out-of-Plane
$\Phi_r^1 = 41.800$	$\Phi_{ti}^1 = 15.200$	$\Phi_{to}^1 = 10.200$
$\Phi_r^2 = 7.600$	$\Phi_{ti}^2 = -4.350$	$\Phi_{to}^2 = -1.080$
$\Phi_r^3 = -0.150$	$\Phi_{ti}^3 = 3.390$	$\Phi_{to}^3 = 0.995$
$\Phi_r^4 = 0.690$	$\Phi_{ti}^4 = -0.190$	$\Phi_{to}^4 = -0.550$

Here, we consider an approximation including fourth nearest neighbours, following [55].

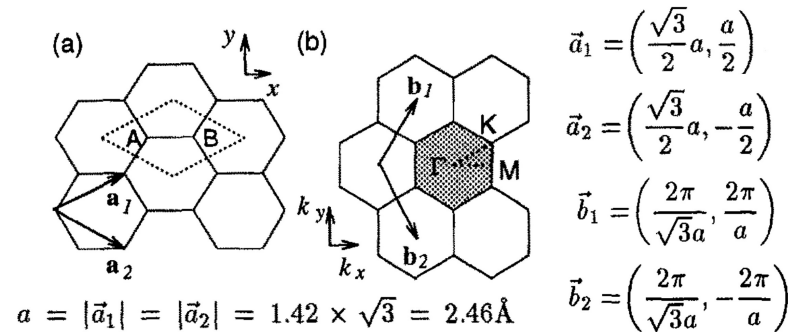


**Figure 16.** Graphene lattice and reciprocal lattice,  $\{\vec{a}_1, \vec{a}_2\}$  and  $\{\vec{b}_1, \vec{b}_2\}$  basis and reciprocal basis vectors, respectively.

As regards phonon interactions, we consider the isotope scattering (is), the edge roughness scattering (rs), the umklapp and normal phonon–phonon scattering (us and ns, respectively), and the scattering related to the under-coordinated atoms present at the longitudinal edges of GNRs (bs).

The edge roughness relaxation time has the form [56]:

$$\left(\tau_p^{(rs)}\right)^{-1}(\mathbf{q}) = \left[\frac{1 - p(\mathbf{q})}{1 + p(\mathbf{q})}\right] \frac{|v_{p,\perp}|}{2L_y}, \tag{15}$$

where  $L_y$  is the nanoribbon width,  $v_{p,\perp}$  represents the phonon velocity component perpendicular to its idealized smooth edge and  $p(\mathbf{q})$  is the specularity parameter:

$$p(\mathbf{q}) = \exp(-4|\mathbf{q}|^2 \Delta^2 \cos^2 \theta_E),$$

with  $\Delta$  the rms height of edge variations and  $\theta_E$  the angle between the normal to the ideal nanoribbon edge and  $\mathbf{q}$ . The specularity parameter, in the form given by (15), manages to capture the details of the interaction between each phonon mode and the edge roughness [56]. In particular, it can discern the different thermal conductivity of armchair- and zigzag-GNRs (AGNR and ZGNR), due to their different rms heights, as can be seen below.

The isotope scattering is due, as said, to the presence of a percentage of different isotopes, and its reciprocal relaxation time, in the 2-D case, reads

$$\left(\tau_p^{(is)}\right)^{-1}(\mathbf{q}) = \frac{\pi}{2\hbar^2} \Gamma \mathcal{A}_0 \epsilon_p^2 D_p(\epsilon_p),$$

where  $\mathcal{A}_0$  is the average area occupied by a carbon atom, and  $D_p(\epsilon_p)$  is the phonon density of states, which is expressed by

$$D_p(\epsilon) = \frac{1}{(2\pi)^2} \int \frac{dL_p(\epsilon)}{|\mathbf{v}_p|},$$

where integration is in the wave vector plane, along the isoenergy curve with energy  $\epsilon$ ,  $dL_p(\epsilon)$  being its infinitesimal length–element,  $p = LA, TA, ZA$ . We remind that the transversal out of plane vibrations, whose displacement vector is along the  $z$ -axis, are called flexural modes (ZA).

The scattering related to the under-coordinated atoms at the  $y$ -edges of the nanoribbons has been taken into account only recently [57–59]. Due to the shorter and stronger bonds of these atoms, a perturbing potential is generated whose effect can be taken into account as a further phonon scattering mechanism. Its reciprocal relaxation time is:

$$(\tau_p^{bd})^{-1} = \frac{4\pi}{\hbar^2} \frac{N_U}{N} \Omega_0 \left( \frac{\delta k}{k} \right)^2 \epsilon_p^2 D_p(\epsilon_p),$$

$k$  being the bond force constant,  $\frac{N_U}{N}$  the ratio between the number of under-coordinated atoms and the total number of atoms,  $\Omega_0$  the area of the primitive cell, and  $\delta k$  the change of the force constant for the under-coordinated atoms. A dimensionality analysis gives:

$$k = k(z) \propto \frac{E(z)}{d^2(z)}; \tag{16}$$

here,  $z$  is the effective atomic coordination number, equal to 3 for graphene carbon atoms, and

$$E(z) = \left( \frac{d_0}{d(z)} \right)^m E_b, \quad d(z) = \frac{2d_0}{1 + e^{\frac{12-z}{8z}}}. \tag{17}$$

$E(z)$ ,  $E_b$ ,  $d(z)$  and  $d_0$  are the bond energy, its single bond bulk value, the bond length and its bulk value, respectively. The parameter  $m$  characterizes the bond nature, for carbonium  $m = 2.56$ . From (16) and (17), one gets:

$$(\tau_p^{bd})^{-1} = \frac{4\pi}{\hbar^2} \frac{N_U}{N} \Omega_0 \left[ \left( \frac{1 + e^{\frac{13-z}{8z-8}}}{\frac{12-z}{8z}} \right)^{m+2} - 1 \right]^2 \epsilon_p^2 D_p(\epsilon_p).$$

The ratio  $\frac{N_U}{N}$  as a function of the GNR width is given by:

$$\frac{N_U}{N} = \begin{cases} \frac{6a_0}{2\sqrt{3}L_y + 3a_0}, & \text{AGNR} \\ \frac{3a_0}{2L_y + 3a_0}, & \text{ZGNR}, \end{cases}$$

with  $a_0 = 0.246$  nm the graphene lattice constant.

Eventually, the reciprocal umklapp relaxation time is the same as that in the 3D case and, for all branches of phonons, the normal one has the same form as that for the transversal acoustical phonons of 3D materials. We also underline that the approximation for the normal scattering collision operator, which was first introduced by Callaway, is really crucial since, in 2D materials, the normal scattering is dominant over the umklapp one, and it is necessary to ensure the momentum conservation in order not to underestimate the thermal conductivity [1,60,61]. The values of the parameters appearing in the relaxation times are reported in Table 5.

In the computation of the integrals present in the closure relations, we need the next Properties.

**Table 5.** Physical parameters for Graphene.

Parameter	Value	Parameter	Value
$v_{LA}$	21.9 nm/ps	$\theta_{LA}$	1826.39 K
$v_{TA}$	11.7 nm/ps	$\theta_{TA}$	1126.18 K
$v_{ZA}$	2.28 nm/ps	$\theta_{ZA}$	623.62 K
$\gamma_{LA}$	2	$M_{C_{12}}$	$1.99 \times 10^{-27}$ Kg
$\gamma_{TA}$	2/3	$M_{C_{13}}$	$2.16 \times 10^{-26}$ Kg
$\gamma_{ZA}$	-3/2	$\mathcal{A}_0$	$2.62 \times 10^{-20}$ m <sup>2</sup>

**Property 1.** Let  $F(\epsilon)$  be an integrable function of the phonon energy  $\epsilon$ , one has:

$$\int_B F(\epsilon) d\mathbf{q} = 12 \int_{B_1} F(\epsilon) d\mathbf{q},$$

where  $B_1$  is the irreducible wedge of the first Brillouin zone consisting of the triangle of vertices  $\Gamma$ ,  $M$  and  $K$ , see Figure 16.

**Property 2.** Let  $\mathbf{v}$  be the phonon group velocity, one has:

$$\begin{aligned} \int_B v_1^2 F(\epsilon) d\mathbf{q} &= \int_B v_2^2 F(\epsilon) d\mathbf{q} = \Phi_1^{vv}(F) := 4 \left\{ \left[ 2\mathcal{R}_{11}^2 + 1 \right] \int_{B_1} v_1^2 F(\epsilon) d\mathbf{q} \right. \\ &\quad \left. + 2\mathcal{R}_{12}^2 \int_{B_1} v_2^2 F(\epsilon) d\mathbf{q} \right\} = 6 \int_{B_1} (v_1^2 + v_2^2) F(\epsilon) d\mathbf{q}, \\ \int_B v_1 v_2 F(\epsilon) d\mathbf{q} &= 0, \\ \int_B q_1^2 F(\epsilon) d\mathbf{q} &= \int_B q_2^2 F(\epsilon) d\mathbf{q} = \Phi_1^{qq}(F) := 6 \int_{B_1} (q_1^2 + q_2^2) F(\epsilon) d\mathbf{q}, \\ \int_B q_1 q_2 F(\epsilon) d\mathbf{q} &= 0, \\ \int_B q_1 v_1 F(\epsilon) d\mathbf{q} &= \int_B q_2 v_2 F(\epsilon) d\mathbf{q} = \Phi_1^{qv}(F) := 6 \int_{B_1} (q_1 v_1 + q_2 v_2) F(\epsilon) d\mathbf{q}, \\ \int_B q_1 v_2 F(\epsilon) d\mathbf{q} &= \int_B q_2 v_1 F(\epsilon) d\mathbf{q} = 0, \end{aligned}$$

where the matrix

$$\mathcal{R} = \begin{pmatrix} \cos(\pi/3) & -\sin(\pi/3) \\ \sin(\pi/3) & \cos(\pi/3) \end{pmatrix},$$

rotates the plane by an angle of  $\pi/3$ .

**Property 3.** Let  $G_e(\mathbf{v})$  be an even function both of  $v_1$  and  $v_2$ , one has:

$$\begin{aligned} \int_B v_i^2 G_e(\mathbf{v}) d\mathbf{q} = \Phi_{2,i}(G_e) &:= 4 \sum_{r=1}^2 \sum_{s=1}^2 \left\{ \int_{B_1} v_r^2 G_e(\mathbf{v}) d\mathbf{q} \right. \\ &\quad \left. + \mathcal{R}_{ir} \mathcal{R}_{is} \int_{B_1} (v_r' v_s' G_e(\mathcal{R}\mathbf{v}') + v_r v_s G_e(\mathcal{R}\mathbf{v})) d\mathbf{q} \right\}, \\ \int_B v_i v_j G_e(\mathbf{v}) d\mathbf{q} &= 0, \quad i \neq j, \end{aligned}$$

with  $\mathbf{v}' = \begin{pmatrix} v_1 \\ -v_2 \end{pmatrix}$ .

**Property 4.** The relaxation times are either even functions ( $\tau_p^{(is)}, \tau_\alpha^{(pps)}, \tau_p^{(bs)}$ ) of the energy or even functions ( $\tau_p^{(rs)}$ ) of both the components of  $\mathbf{v}$ .

The above-written  $\Phi_1, \Phi_{2,i}, i = 1, 2$  are functionals over a suitable space of functions defined on B.

The previous properties are a consequence of the hexagon’s symmetries, which make  $\epsilon$  even with respect both to  $q_1$  and  $q_2$ , and invariant under rotations in the wave-vector plane of angles multiples of  $\pi/3$ . It also descends that  $\mathbf{v}$  is odd with respect both to  $q_1$  and  $q_2$ , and

$$\mathbf{v}(\mathcal{R}^m \mathbf{q}) = \mathcal{R}^m \mathbf{v}(\mathbf{q}), \quad \forall \mathbf{q} \in B_1, m \in \mathbb{Z}.$$

Exploiting the previous properties, it is possible to find:

$$\begin{aligned} \tilde{K}_M^p &= y_p \Phi_1^{vv} \left( \frac{\epsilon_p^{\tilde{M}(M)}}{\exp(\epsilon_p/K_B T) - 1} \right), \\ a_{MN}^p &= -y_p \Phi_1^{vv} \left( \epsilon_p^{\tilde{M}(M)+\tilde{M}(N)} \frac{\exp(\epsilon_p/K_B T)}{(\exp(\epsilon_p/K_B T) - 1)^2} \right), \\ q_{MN}^p &= y_p \left[ \sum_{l=is,bs}^{us,ns} \Phi_1^{vv} \left( \epsilon_p^{\tilde{M}(M)+\tilde{M}(N)} \frac{\exp(\epsilon_p/K_B T)}{\tau_p^l (\exp(\epsilon_p/K_B T) - 1)^2} \right) \right. \\ &+ \Phi_2 \left( \epsilon_p^{\tilde{M}(M)+\tilde{M}(N)} \frac{\exp(\epsilon_p/K_B T)}{\tau_p^{rs} (\exp(\epsilon_p/K_B T) - 1)^2} \right) \\ &- \left. \frac{\Phi_1^{vq} \left( \epsilon_p^{\tilde{M}(N)} \frac{\exp(\epsilon_p/K_B T)}{\tau_p^{ns} (\exp(\epsilon_p/K_B T) - 1)^2} \right) \Phi_1^{vq} \left( \epsilon_p^{\tilde{M}(M)} \frac{\exp(\epsilon_p/K_B T)}{\tau_p^{ms} (\exp(\epsilon_p/K_B T) - 1)^2} \right)}{\Phi_1^{qq} \left( \frac{\exp(\epsilon_p/K_B T)}{\tau_p^{ms} (\exp(\epsilon_p/K_B T) - 1)^2} \right)} \right]. \end{aligned}$$

We underline that, in the 2-D case, the formula based on the hierarchy of macroscopic models presents a significant advantage with respect to the commonly used Formulas (5) and (6). In fact, the integrand functions in (12) are integrable also in the two-dimensional case, which means that no truncation procedures [53] are required for computing of the closure integrals even in the case when one considers only the isotope and phonon-phonon scatterings. All the results are obtained by using nine vector moments, with integer powers of the microscopic energy, since, as is shown in Figure 17 (left), the convergence can be considered attained with this number of moments. Figures 17–20 show the steady-state thermal conductivity. Figure 17 represents the bulk conductivity, around the room temperature it reaches very high values, in the order of thousands of W/Km, corresponding to the ballistic limit for suspended graphene, which is estimated in Figure 3d of [53], see also [1,6,60]. As can be seen in the right part of the figure, the normal scattering plays a significant role in all temperature ranges, except for low temperatures, in fact, it reduces the thermal conductivity by a half at the room temperature and by even more at higher temperatures.

In Figure 18, the thermal conductivity of 80 nm wide GNRs is depicted, on the left it is derived by ignoring the phonon interaction with the potential generated by the under-coordinated atoms. The rms heights of edge variations of A- and ZGNRs have been considered equal to 0.06 nm and 0.02 nm, respectively. It is possible to see that the ZGNR’s thermal conductivity is significantly higher, of up to one order of magnitude, and that for both types of NRs the edge scattering plays a relevant role up to temperatures of around

700 K, which is consistent with molecular dynamics simulations. In particular, the thermal conductivity is lower along the width direction, for example, at  $T = 300$  K the ZGNR's conductivity is reduced of 10% along the x-direction and of 27% along the y-direction, while for AGNRs the reductions respectively are 54% and 75%. The same holds true also for thinner nanoribbons except that the temperature up to which es scattering is relevant increases, as is shown in Figure 19, on the left.

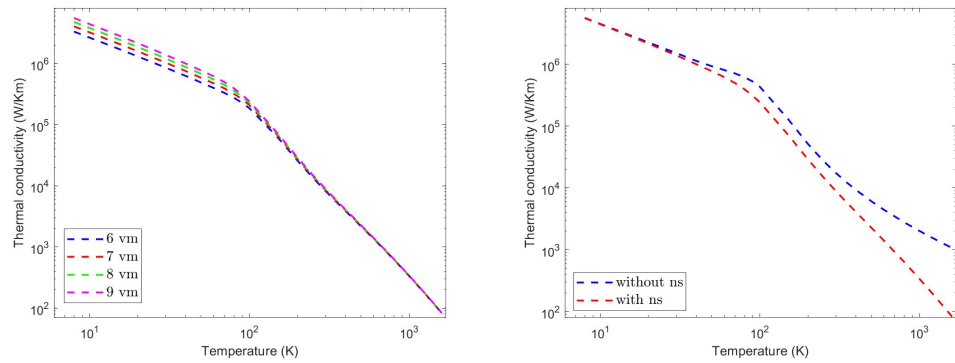


**Figure 17.** (Left): The steady-state conductivity for bulk graphene (without es scattering), obtained by using different numbers of vector moments (vm). (Right): with and without normal scattering. The fractions of  $C_{12}$  and  $C_{13}$  are  $f_{C_{12}} = 0.989\%$ ,  $f_{C_{13}} = 0.011\%$ .

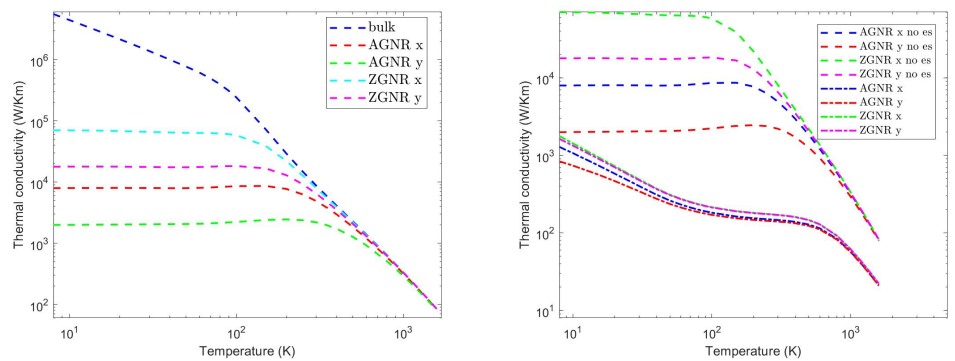


**Figure 18.** The steady-state thermal conductivity for A- and ZGNRs in the x- and y-direction. (Left): only with edge scattering. (Right): with and without bs-scattering.  $L_y = 80$  nm.

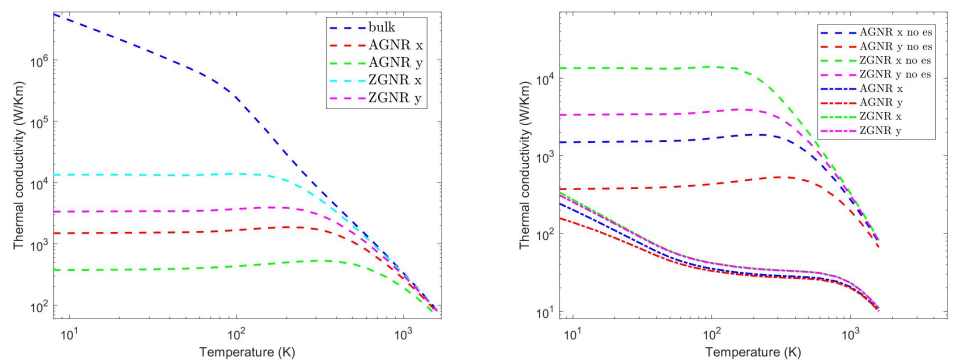
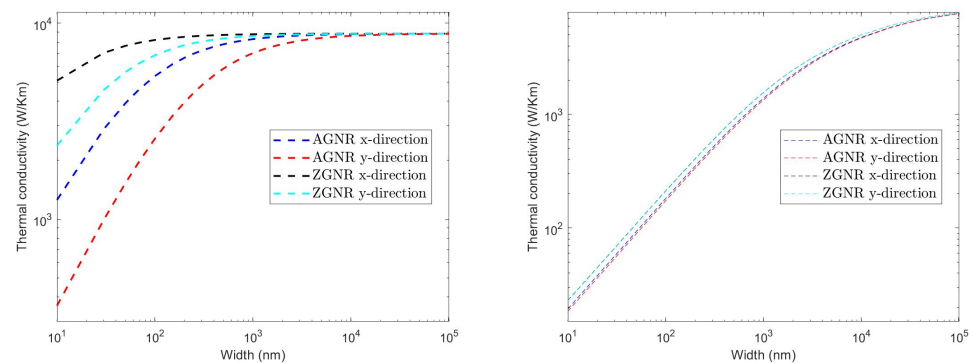


**Figure 19.** The steady-state thermal conductivity for A- and ZGNRs in the x- and y-direction. (Left): only with edge scattering. (Right): with and without bs-scattering.  $L_y = 15$  nm.

The thermal conductivity is drastically reduced, of around two order of magnitudes, when one includes also the scattering by under-coordinated atoms, as reported in the

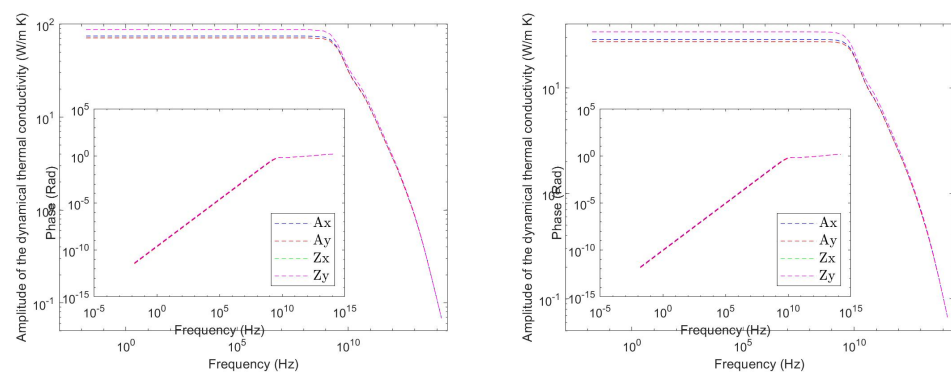
right sides of Figures 18 and 19, and this happens almost independently of the type of nanoribbon and of the direction, and at all temperatures.

The significance of the bs-scattering is also supported by the trend of the thermal conductivity, at  $T = 300$  K, as a function of the width, which is depicted in Figure 20, on the left with only the es scattering, and on the right with the es and bs scatterings. It is possible to see that the thermal conductivity goes to saturation at  $L_y \approx 100$  nm, and that the effect of the bs-scattering is more pronounced than that of the es one at all widths.



**Figure 20.** The steady-state thermal conductivity for A and ZGNRs in the x- and y-direction vs the nanoribbon width. (Left): with only the es-scattering. (Right): with the es- and bs-scatterings.  $T = 300$  K.

Concerning the dynamical conductivity, in Figure 21 it is shown its amplitude and phase in the x- and y-direction for nanoribbons with widths of 40 nm and 15 nm respectively, at a temperature  $T = 300$  K. For both widths the conductivity holds constant at low frequencies and begins to fall rapidly at higher frequencies. The phase starts increasing at higher frequencies up to the saturation value of  $\frac{\pi}{2}$ . The cut-off frequency for armchair and zig-zag nanoribbons of width equal to 40 nm, for various values of the temperature, is reported in Table 6.

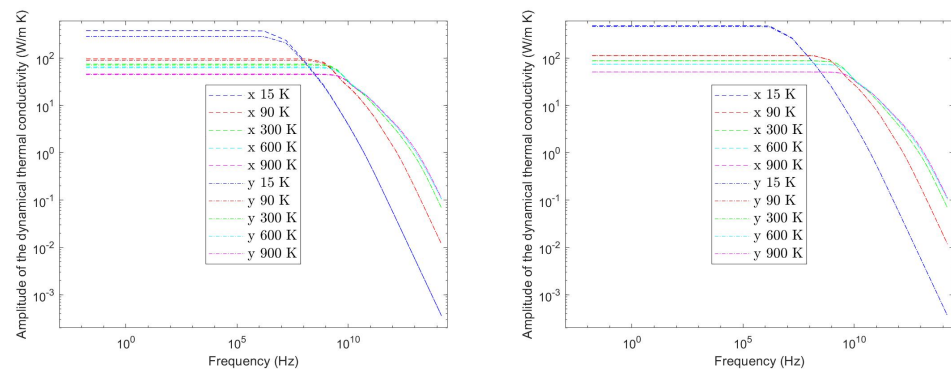


**Figure 21.** The amplitude and the phase of the dynamical thermal conductivity for GNRs, in the x- and y-direction. (Left):  $L_y = 40$  nm. (Right):  $L_y = 15$  nm.

It increases with increasing  $T$  as can also be seen in Figure 22, which represents the trend of the amplitude of the thermal conductivity at some values of the temperature. For values higher than the cut-off frequency, one still has  $|\kappa| \sim \frac{1}{f}$ . Like in silicon and germanium, the phonon modes whose scattering rates are smaller than the frequency of temperature disturbances contribute to thermal conductivity less than in the steady state, and for this reason the dynamical thermal conductivity exhibits a low-pass thermal filter behavior [62].

**Table 6.** Cut-off frequency vs temperature in the y-direction.

Temperature (K)	AGNR $f_c$ ( $10^{10}$ Hz)	ZGNR $f_c$ ( $10^{10}$ Hz)
15	0.0017	0.0012
90	0.1475	0.1155
300	0.4051	0.3275
600	0.5509	0.4627
900	0.9389	0.8512

**Figure 22.** Amplitude of the dynamical conductivity in the x- and y-directions for an armchair (left) and zig-zag (right) GNR with width equal to 40 nm.

## 7. Conclusions

In this paper, we have reviewed some results on thermal conductivity of silicon, germanium and graphene recently obtained by using a formula derived from a hierarchy of macroscopic models for heat transport in semiconductors [20–22]. The macroscopic models are retrieved from the Boltzmann–Peierls equation by using the moments method. The moments chosen as state variables are the phonon energies and a suitable number of vector moments, which include the heat fluxes. The equations have been closed by exploiting the maximum entropy principle. The results are recast in a form which is suitable for both 3D and 2D materials and we examine the main characteristics of the thermal conductivity in semiconductors. The influence of all the main scattering mechanisms is taken into account and also, in the case of silicon–germanium alloys, the possibility of reducing the thermal conductivity by embedding nanoparticles in the matrix. In the case of graphene, the recently introduced scattering by underco-ordinated atoms is analysed. For the dynamical conductivity, it is confirmed that, at high frequencies, materials exhibit a low-pass thermal filter behavior. This review paper can be considered a natural continuation of a previous review paper [23] and together they confirm that MEP is a physically sound method for devising macroscopic models for charge and energy transport in semiconductor materials.

**Funding:** This research received no external funding.

**Institutional Review Board Statement:** Not applicable.

**Informed Consent Statement:** Not applicable.

**Acknowledgments:** The author acknowledges support by GNFM (INDAM) and by the Department of Mathematics and Computer Science of the University of Calabria.

**Conflicts of Interest:** The author declares no conflict of interest.

## References

1. Fugallo, G.; Cepellotti, A.; Paulatto, L.; Lazzeri, M.; Mauri, F.; Marzari, N. Thermal Conductivity of Graphene and Graphite: Collective Excitations and Mean Free Paths. *Nano Lett.* **2014**, *14*, 6109. [[CrossRef](#)]
2. Ezzahri, Y.; Joulain, K. Dynamical thermal conductivity of bulk semiconductor crystals. *J. Appl. Phys.* **2012**, *112*, 8. [[CrossRef](#)]

3. Ezzahri, Y.; Joulain, K. Effect of embedding nanoparticles on the lattice thermal conductivity of bulk semiconductor crystals. *Appl. Phys.* **2013**, *113*, 043510. [[CrossRef](#)]
4. Mei, S.; Maurer, L.N.; Aksamija, Z.; Knezevic, I. Full-dispersion Monte Carlo simulation of phonon transport in micron-sized graphene nanoribbons. *J. Appl. Phys.* **2014**, *116*, 164307-1–164307-17. [[CrossRef](#)]
5. Morelli, D.T.; Heremans, J.P.; Slack, G.A. Estimation of the isotope effect on the lattice thermal conductivity of group IV and group III-IV semiconductors. *Phys. Rev. B* **2002**, *66*, 195304. [[CrossRef](#)]
6. Nika, D.L.; Pokatilov, E.P.; Askerov, A.S.; Balandin, A.A. Phonon thermal conduction in graphene: Role of Umklapp and edge roughness scattering. *Phys. Rev. B* **2009**, *79*, 155413. [[CrossRef](#)]
7. Ruf, T.; Henn, R.W.; Asen-Palmer, M.; Gmelin, E.; Cardona, M.; Pohl, H.-J.; Devyatych, G.G.; Sennikov, P.G. Thermal conductivity of isotopically enriched silicon. *Solid State Commun.* **2000**, *115*, 243. [[CrossRef](#)]
8. Volz, S.G. Thermal Insulating Behavior in Crystals at High Frequencies. *Phys. Rev. Lett.* **2001**, *87*, 074301. [[CrossRef](#)]
9. Ye, Z.Q.; Cao, B.Y.; Yao, W.J.; Feng, T.; Ruan, X. Spectral phonon thermal properties in graphene nanoribbons. *Carbon* **2015**, *93*, 915–923. [[CrossRef](#)]
10. Balandin, A.A.; Ghosh, S.; Nika, D.L.; Pokatilov, E.P. Thermal Conduction in Suspended Graphene Layers. *Fuller. Nanotub. Carbon Nanostructures* **2010**, *18*, 474–486. [[CrossRef](#)]
11. Pop, E.; Goodson, K.E. Thermal Phenomena in Nanoscale Transistors. *J. Electron. Packag.* **2006**, *78*, 102–108. [[CrossRef](#)]
12. Wu, T.; Wu, Z.; He, Y.; Zhu, Z.; Wang, L.; Yin, K. Femtosecond laser textured porous nanowire structured glass for enhanced thermal imaging. *Chin. Opt. Lett.* **2022**, *3*, 033801. [[CrossRef](#)]
13. Kim, W.; Zide, J.; Gossard, A.; Klenov, D.; Stemmer, S. Thermal Conductivity Reduction and Thermoelectric Figure of Merit Increase by Embedding Nanoparticles in Crystalline Semiconductors. *PRL* **2006**, *96*, 045901-1-4. [[CrossRef](#)]
14. Ghosh, S.; Calizo, I.; Teweldebrhan, D.; Pokatilov, E.P.; Nika, D.L.; Balandin, A.A.; Bao, W.; Miao, F.; Lau, C.N. Extremely high thermal conductivity of graphene: Prospects for thermal management applications in nanoelectronic circuits. *Appl. Phys. Lett.* **2008**, *92*, 151911. [[CrossRef](#)]
15. Callaway, J. Model for Lattice Thermal Conductivity at Low Temperatures. *Phys. Rev.* **1959**, *113*, 1046. [[CrossRef](#)]
16. Holland, M.G. Analysis of Lattice Thermal Conductivity. *Phys. Rev.* **1963**, *132*, 2461. [[CrossRef](#)]
17. Peirls, R. *Quantum Theory of Solids*; Oxford University Press: Oxford, UK, 1955.
18. Neto, A.H.C.; Guinea, F.; Peres, N.M.R.; Novoselov, K.S.; Geim, A.K. The electronic properties of graphene. *Rev. Modern Phys.* **2009**, *81*, 109. [[CrossRef](#)]
19. Aksamijaa, Z.; Knezevic, I. Lattice thermal conductivity of graphene nanoribbons: Anisotropy and edge roughness scattering. *Appl. Phys. Lett.* **2011**, *98*, 141919. [[CrossRef](#)]
20. Mascali, G. A new formula for thermal conductivity based on a hierarchy of hydrodynamical models. *J. Stat. Phys.* **2016**, *163*, 1268–1284. [[CrossRef](#)]
21. Mascali, G.; Romano, V. A hierarchy of macroscopic models for phonon transport in graphene. *Phys. A Stat. Mech. Its Appl.* **2020**, *548*, 124489. [[CrossRef](#)]
22. Mascali, G. Thermal conductivity reduction by embedding nanoparticles. *J. Comput. Electron.* **2017**, *16*, 180–189. [[CrossRef](#)]
23. Mascali, G.; Romano, V. Exploitation of the maximum entropy principle in the mathematical modeling of charge transport in semiconductors. *Entropy* **2017**, *19*, 36 [[CrossRef](#)]
24. Landau, L.D.; Lifschitz, E.M. *Statistical Physics*; Part 1; Pergamon Press: Oxford, UK; New York, NY, USA, 1980; Volume 5.
25. Kadanoff, L.P.; Baym, G. *Quantum Statistical Mechanics*; CRC Press: Boca Raton, FL, USA; London, UK; New York, NY, USA, 1962.
26. Klemens, P.G. Anharmonic decay of optical phonons. *Phys. Rev.* **1966**, *148*, 845. [[CrossRef](#)]
27. Mascali, G. A hydrodynamic model for silicon semiconductors including crystal heating. *Eur. J. Appl. Math.* **2015**, *26*, 477. [[CrossRef](#)]
28. Dreyer, W.; Struchtrup, H. Heat pulse experiment revisited. *Continuum Mech. Therm.* **1993**, *5*, 3. [[CrossRef](#)]
29. Struchtrup, H. The BGK-model with velocity-dependent collision frequency. *Continuum Mech. Thermodyn.* **1997**, *9*, 23. [[CrossRef](#)]
30. Camiola, V.D.; Mascali, G.; Romano, V. *Charge Transport in Low Dimensional Structures: The Maximum Entropy Approach*; Springer: Berlin/Heidelberg, Germany, 2020.
31. Mascali, G.; Romano, V. Hydrodynamic subband model for semiconductors based on the maximum entropy principle. *Nuovo C. Della Soc. Ital. Fis.* **2010**, *33*, 155–163.
32. Müller, I.; Ruggeri, T. *Rational Extended Thermodynamics*; Springer: Berlin/Heidelberg, Germany, 1998.
33. Muscato, O.; Castiglione, T. A hydrodynamic model for silicon nanowires based on the maximum entropy principle. *Entropy* **2016**, *18*, 368. [[CrossRef](#)]
34. Muscato, O.; Castiglione, T.; Coco, A. Hydrodynamic modeling of electron transport in gated silicon nanowires transistors. *Phys. Math. Nat. Sci.* **2019**, *97*, (Suppl. 1), A18.
35. Muscato, O.; Di Stefano, V.D. A hierarchy of hydrodynamic models for silicon carbide semiconductors. *Commun. Appl. Ind. Math.* **2017**, *8*, 251–264. [[CrossRef](#)]
36. Lebon, G.; Jou, D.; Casa-Vazquez, J. *Understanding Non-equilibrium Thermodynamics*; Springer: Berlin/Heidelberg, Germany, 2008.
37. Reinecke, S.; Kremer, G.M. Method of moments of Grad. *Phys. Rev. A* **1990**, *42*, 815. [[CrossRef](#)] [[PubMed](#)]
38. Pop, E.; Dutton, R.W.; Goodson, K.E. Analytic band Monte Carlo model for electron transport in Si including acoustic and optical phonon dispersion. *J. App. Phys.* **2004**, *96*, 4998–5005 [[CrossRef](#)]

39. Kundu, A.; Mingo, N.; Broido, D.A.; Stewart, D.A. Role of light and heavy embedded nanoparticles on the thermal conductivity of SiGe alloys. *Phys. Rev. B* **2011**, *84*, 125426-1. [[CrossRef](#)]
40. Mingo, N.; Hauser, D.; Kobayashi, N.P.; Plissonnier, M.; Shakouri, A. "Nanoparticle-in-Alloy" Approach to Efficient Thermoelectrics: Silicides in SiGe. *Nano Lett.* **2009**, *9*, 711–715. [[CrossRef](#)] [[PubMed](#)]
41. Barletti, L.; Negulescu, C. Quantum Transmission Conditions for Diffusive Transport in Graphene with Steep Potentials. *J. Stat. Phys.* **2018**, *171*, 696–726. [[CrossRef](#)]
42. Freitag, M. Nanoelectronics goes flat out. *Nat. Nanotechnol.* **2008**, *3*, 455–457. [[CrossRef](#)]
43. Fischetti, M.V.; Kim, J.; Narayanan, S.; Ong, Z.; Sachs, C.; Ferry, D.K.; Aboud, S.J. Pseudopotential-based studies of electron transport in graphene and graphene nanoribbons. *J. Phys. Condens. Matter* **2013**, *25*, 473202. [[CrossRef](#)]
44. Lichtenberger, P.; Morandi, O.; Schürer, F. High-field transport and optical phonon scattering in graphene. *Phys. Rev. B* **2011**, *84*, 045406. [[CrossRef](#)]
45. Luca, L.; Romano, V. Quantum corrected hydrodynamic models for charge transport in graphene. *Ann. Phys.* **2019**, *406*, 30–53. [[CrossRef](#)]
46. Mascali, G.; Romano, V. Charge transport in graphene including thermal effects. *SIAM J. Appl. Math.* **2017**, *77*, 593–613. [[CrossRef](#)]
47. Morandi, O. Charge transport and hot-phonon activation in graphene. *J. Comput. Theor. Transp.* **2014**, *43*, 162–182. [[CrossRef](#)]
48. Nastasi, G.; Camiola, V.D.; Romano, V. Direct Simulation of Charge Transport in Graphene Nanoribbons. *Commun. Comput. Phys.* **2022**, *31*, 449–494. [[CrossRef](#)]
49. Nastasi, G.; Romano, V. An Efficient GFET Structure. *IEEE Trans. Electron Devices* **2021**, *68*, 4729–4734. [[CrossRef](#)]
50. Novoselov, K.S.; Geim, A.K.; Morozov, S.V.; Jiang, D.; Katsnelson, M.I.; Grigorieva, I.V.; Dubonos, S.V.; Firsov, A.A. Two-dimensional gas of massless Dirac fermions in graphene. *Nature* **2005**, *438*, 197. [[CrossRef](#)]
51. Zamponi, N.; Barletti, L. Hydrodynamic equations for electrons in graphene obtained from the maximum entropy principle. *Math. Methods Appl. Sci.* **2011**, *34*, 807–818. [[CrossRef](#)]
52. Zou, J.H.; Xu, X.T.; Cao, B.Y. Size-dependent mode contributions to the thermal transport of suspended and supported graphene. *Appl. Phys. Lett.* **2019**, *115*, 123105. [[CrossRef](#)]
53. Pop, E.; Varshney, V.; Roy, A.K. Thermal properties of graphene: Fundamentals and applications. *MRS Bull.* **2012**, *37*, 1273. [[CrossRef](#)]
54. Yin, K.; Wang, L.; Deng, Q.; Huang, Q.J.; Li, Q.; He, J. Femtosecond Laser Thermal Accumulation-Triggered Micro-/Nanostructures with Patternable and Controllable Wettability Towards Liquid Manipulating. *Nano-Micro Lett.* **2022**, *14*, 97. [[CrossRef](#)]
55. Saito, R.; Dresselhaus, G.; Dresselhaus, M.S. *Physical Properties of Carbon Nanotubes*; Imperial College Press: London, UK, 1998.
56. Bae, M.H.; Li, Z.; Aksamija, Z.; Martin, P.N.; Xiong, F.; Ong, Z.Y.; Knezevic, I.; Pop, E. Ballistic to diffusive crossover of heat flow in graphene ribbons. *Nat. Commun.* **2013**, *4*, 1734. [[CrossRef](#)]
57. Wang, Y.; Qiu, B.; Ruan, X. Edge effect on thermal transport in graphene nanoribbons: A phonon localization mechanism beyond edge roughness scattering. *Appl. Phys. Lett.* **2012**, *101*, 013101. [[CrossRef](#)]
58. Xie, G.; Ju, Z.; Zhou, K.; Wei, X.; Guo, Z.; Cai, Y.; Zhang, G. Ultra-low thermal conductivity of two-dimensional phononic crystals in the incoherent regime. *NPJ Comput. Mater.* **2018**, *4*, 21. [[CrossRef](#)]
59. Xie, G.; Shen, Y.; Wei, X.; Yang, L.; Xiao, H.; Zhong, J.; Zhang, G. A Bond-order Theory on the Phonon Scattering by Vacancies in Two-dimensional Materials. *Sci. Rep.* **2014**, *4*, 5085. [[CrossRef](#)] [[PubMed](#)]
60. Fugallo, G.; Cepellotti, A.; Paulatto, L.; Lazzeri, M.; Mauri, F.; Marzari, N. Phonon hydrodynamics in two-dimensional materials. *Nat. Commun.* **2015**, *6*, 6400.
61. Lindsay, L.; Li, W.; Carrete, J.; Mingo, N.; Broido, D.A.; Reinecke, T.L. Phonon thermal transport in strained and unstrained graphene from first principles. *Phys. Rev. B* **2014**, *89*, 155426. [[CrossRef](#)]
62. Majee, A.K.; Aksamija, Z. Dynamical thermal conductivity of suspended graphene ribbons in the hydrodynamic regime. *Phys. Rev. B* **2018**, *98*, 024303. [[CrossRef](#)]